universe

IMPACT FACTOR 2.813

CITESCORE 3.2

Article

A Reanalysis of the Latest SH0ES Data for H_0: Effects of New Degrees of Freedom on the Hubble Tension

Leandros Perivolaropoulos and Foteini Skara

Special Issue

Dark Matter and Dark Energy: Particle Physics, Cosmology, and Experimental Searches

Edited by

Dr. Sunny Vagnozzi, Dr. Eleonora Di Valentino, Prof. Alessandro Melchiorri, Prof. Olga Mena and Dr. Luca Visinelli

MDPI

https://doi.org/10.3390/universe8100502

universe

MDPI

Article

A Reanalysis of the Latest SH0ES Data for H_0: Effects of New Degrees of Freedom on the Hubble Tension

Leandros Perivolaropoulos * and Foteini Skara

Department of Physics, University of Ioannina, 45110 Ioannina, Greece
* Correspondence: Leandros@uoi.gr

Abstract: We reanalyze in a simple and comprehensive manner the recently released SH0ES data for the determination of H_0. We focus on testing the homogeneity of the Cepheid+SnIa sample and the robustness of the results in the presence of new degrees of freedom in the modeling of Cepheids and SnIa. We thus focus on the four modeling parameters of the analysis: the fiducial luminosity of SnIa M_B and Cepheids M_W and the two parameters (b_W and Z_W) standardizing Cepheid luminosities with period and metallicity. After reproducing the SH0ES baseline model results, we allow for a transition of the value of any one of these parameters at a given distance D_c or cosmic time t_c, thus adding a single degree of freedom in the analysis. When the SnIa absolute magnitude M_B is allowed to have a transition at $D_c \simeq 50$ Mpc (about 160 Myrs ago), the best-fit value of the Hubble parameter drops from $H_0 = 73.04 \pm 1.04$ km s^{-1} Mpc^{-1} to $H_0 = 67.32 \pm 4.64$ km s^{-1} Mpc^{-1} in full consistency with the Planck value. Additionally, the best-fit SnIa absolute magnitude $M_B^>$ for $D > D_c$ drops to the Planck inverse distance ladder value $M_B^> = -19.43 \pm 0.15$, while the low distance best fit $M_B^<$ parameter remains close to the original distance ladder calibrated value $M_B^< = -19.25 \pm 0.03$. Similar hints for a transition behavior is found for the other three main parameters of the analysis (b_W, M_W and Z_W) at the same critical distance $D_c \simeq 50$ Mpc, even though in that case, the best-fit value of H_0 is not significantly affected. When the inverse distance ladder constraint on $M_B^>$ is included in the analysis, the uncertainties for H_0 reduce dramatically ($H_0 = 68.2 \pm 0.8$ km s^{-1} Mpc^{-1}), and the M_B transition model is strongly preferred over the baseline SH0ES model ($\Delta\chi^2 \simeq -15$, $\Delta AIC \simeq -13$) according to the AIC and BIC model selection criteria.

Keywords: Hubble tension; cosmology; galaxies; Cepheid calibrators; gravitational transition; SH0ES data

Citation: Perivolaropoulos, L.; Skara, F. A Reanalysis of the Latest SH0ES Data for H_0: Effects of New Degrees of Freedom on the Hubble Tension. *Universe* **2022**, *8*, 502. https://doi.org/10.3390/universe8100502

Academic Editors: Sunny Vagnozzi, Eleonora Di Valentino, Alessandro Melchiorri, Olga Mena and Luca Visinelli

Received: 31 August 2022
Accepted: 19 September 2022
Published: 25 September 2022

1. Introduction

1.1. The Current Status of the Hubble Tension and Its Four Assumptions

Measurements of the Hubble constant using observations of type Ia supernovae (SnIa) with Cepheid calibrators by the SH0ES team has led to a best-fit value $H_0^{R21} = 73.04 \pm 1.04$ km s^{-1} Mpc^{-1} [1] (hereafter R21). This highly precise but not necessarily accurate measurement is consistent with a wide range of other less precise local measurements of H_0 using alternative SnIa calibrators [2–5], gravitational lensing [6–9], gravitational waves [10–14], gamma-ray bursts as standardizable candles [15–19], quasars as distant standard candles [20], type II supernovae [21,22], $\gamma-$ray attenuation [23], etc. (for recent reviews, see Refs. [24,25]). This measurement is based on two simple assumptions:

- There are no significant systematic errors in the measurements of the properties (period, and metallicity) and luminosities of Cepheid calibrators and SnIa.
- The physical laws involved and the calibration properties of Cepheids and SnIa in all the rungs of the distance ladder are well understood and modeled properly.

This measurement, however, is at 5σ tension (Hubble tension) with the corresponding measurement from *Planck* observations of the CMB angular power spectrum (early time inverse distance ladder measurement) $H_0^{P18} = 67.36 \pm 0.54$ km s^{-1} Mpc^{-1} [26] (see also

Refs. [24,25,27–34] for relevant recent reviews). This inverse distance ladder measurement is also based on two basic assumptions:

- The scale of the sound horizon at the last scattering surface is the one calculated in the context of the standard cosmological model with the known degrees of freedom (cold dark matter, baryons and radiation) and thus, it is a reliable distance calibrator.
- The evolution of the Hubble free expansion rate $E(z) \equiv H(z)/H_0$ from the time of recombination (redshift $z = z_{rec}$) until the present time ($z = 0$) is the one predicted by the standard ΛCDM model as defined by the best-fit Planck parameters (Planck18/ΛCDM) [26,35].

A wide range of approaches have been implemented in efforts to explain this Hubble tension (for reviews, see Refs. [24,25,27,34,36–39]). These approaches introduce new degrees of freedom that violate at least one of the above four assumptions and may be classified in accordance with the particular assumption that they are designed to violate.

Thus, early time sound horizon models introduce new degrees of freedom at the time just before recombination (e.g., early dark energy [36,40–52], radiation [53–56] or modified gravity [57–62]) to change the expansion rate at that time and thus decrease the sound horizon scale r_s (early time distance calibrator) to increase H_0, which is degenerate with r_s, to a value consistent with local measurements.

The mechanism proposed by these models attempts to decrease the scale of the sound horizon at recombination, which can be calculated as

$$r_s = \int_0^{t_*} \frac{c_s(a)}{a(t)} dt = \int_{z_*}^{\infty} \frac{c_s(z)}{H(z;\rho_b,\rho_\gamma,\rho_c)} dz = \int_0^{a_*} \frac{c_s(a)}{a^2 H(a;\rho_b,\rho_\gamma,\rho_c)} da \tag{1}$$

where the recombination redshift z_* corresponds to time t_*; ρ_b, ρ_c and ρ_γ denote the densities for baryon, cold dark matter and radiation (photons), respectively; and c_s is the sound speed in the photon–baryon fluid. The angular scale of the sound horizon is measured by the peak locations of the CMB perturbations angular power spectrum and may be expressed in terms of r_s as

$$\theta_s = \frac{r_s}{d_A} = \frac{H_0 r_s}{c \int_0^{z_*} \frac{dz'}{E(z')}} \tag{2}$$

where d_A is the comoving angular diameter distance to last scattering (at redshift $z \approx 1100$) and $E(z)$ is the dimensionless normalized Hubble parameter, which for a flat ΛCDM model is given by

$$E(z) \equiv \frac{H(z)}{H_0} = \left[\Omega_{0m}(1+z)^3 + (1-\Omega_{0m})\right]^{1/2} \tag{3}$$

Equation (2) indicates that there is a degeneracy between r_s, H_0 and $E(z)$, given the measured value of θ_s. A decrease in r_s would lead to an increase in the predicted value of H_0 (early time models), and a late time deformation of $E(z)$ could lead to an increase in the denominator of Equation (2), leading also to an increase in H_0 (late time models).

Early dark energy models have the problem of predicting the stronger growth of perturbations than implied by dynamical probes, such as redshift space distortion (RSD) and weak lensing (WL) data and thus may worsen the $\Omega_m - \sigma_8$ growth tension [63–72] and reduce consistency with growth data and with other cosmological probes and conjectures [38,39,47–49,72–76]. Thus, a compelling and full resolution of the Hubble tension may require multiple (or other) modifications beyond the scale of the sound horizon predicted by ΛCDM cosmology. Even though these models are severely constrained by various cosmological observables, they currently constitute the most widely studied class of models [42–44,50,77,78].

Late time $H(z)$ deformation models introduce new degrees of freedom (e.g., modified gravity [79–82], dynamical late dark energy [83–96], or interacting dark energy with matter [85,97–101]) to deform $E(z)$ at redshifts $z \sim O(1)$ so that the present time value

of $H(z=0) = H_0$ increases and becomes consistent with the local measurements. This class of models is even more severely constrained [84,102–112] by other cosmological observables (SnIa, BAO and growth of perturbations probes), which tightly constrain any deformation [35] from the Planck18/ΛCDM shape of $E(z) \equiv H(z)/H_0$.

The third approach to the resolution of the Hubble tension is based on a search for possible unaccounted systematic effects, including possible issues in modeling the Cepheid data, such as non-standard dust-induced color correction [113], the impact of outliers [114–116], blending effects, SnIa color properties [117], robustness of the constancy of the SnIa absolute magnitude in the Hubble flow [67,118–134], etc. There is currently a debate about the importance of these potential systematic effects [135–138]. Additionally, the possibility for redshift evolution of the Hubble constant was studied by Ref. [139]. In [139], the Hubble tension was analyzed with a binned analysis on the Pantheon sample of SNe Ia through a multidimensional MCMC analysis. Finally, the need for new standardizable candles with redshift values far beyond the SnIa ($3 \lesssim z \lesssim 9$) was studied (see Refs. [15–19] for gamma-ray bursts and Refs. [140,141] for quasars).

A fourth approach related to the previous one is based on a possible change of the physical laws (e.g., a gravitational transition [142,143]) during the past 200 *Myrs* ($z \lesssim 0.01$) when the light of the Cepheid calibrator hosts was emitted [143–152]. In this context, new degrees of freedom should be allowed for the modeling of either Cepheid calibrators and/or SnIa to allow for the possibility of this physics change. If these degrees of freedom are shown not to be excited by the data, then this approach would also be severely constrained. It is possible, however, that nontrivial values of these new parameters are favored by the data, while, at the same time, the best-fit value of H_0 shifts to a value consistent with the inverse distance ladder measurements of H_0 using the sound horizon at recombination as the calibrator. In this case [146], this class of models would be favored, especially in view of the severe constraints that have been imposed on the other three approaches.

The possible new degrees of freedom that could be allowed in the Cepheid+SnIa modeling analysis are clearly infinite, but the actual choices to be implemented in a generalized analysis may be guided by three principles: *simplicity, physical motivation, and improvement of the quality of fit to the data*.

In a recent analysis [146], using a previous release of the SH0ES data [153–155], we showed that a physically motivated new degree of freedom in the Cepheid calibrator analysis allowing for a transition in one of the Cepheid modeling parameters R_W or M_W is mildly favored by the data and can lead to a reduced best fit value of H_0. Here, we extend that analysis in a detailed and comprehensive manner to a wider range of transition degrees of freedom using the latest publicly available SH0ES data described in R21.

1.2. The New SH0ES Cepheid+SnIa Data

The new Cepheid+SnIa data release and analysis from the SH0ES collaboration in R21 includes a significant increase of the sample of SnIa calibrators from 19 in Ref. [153] to 42. These SnIa reside in 37 hosts observed between 1980 and 2021 in a redshift range $0.0015 \lesssim z < 0.011$ (see Table 1 for a more detailed comparison of the latest SH0ES data release with previous updates). These SnIa are calibrated using Cepheids in the SnIa host galaxies. In turn, Cepheid luminosities are calibrated using geometric methods in calibrator nearby galaxies (anchors). These anchor galaxies include the megamaser host NGC 4258[1], the Milky Way (MW) where distances are measured with several parallaxes, and the Large Magellanic Cloud (LMC) where distances are measured via detached eclipsing binaries [154] as well as two supporting anchor galaxies (*M*31 [157] and the Small Magellanic Cloud (SMC). These supporting galaxies are pure Cepheid hosts and do not host SnIa but host large and well measured Cepheid samples. However, geometric measurements of their distances are not so reliable and thus are not directly used in the analysis[2]. The calibrated SnIa in the Hubble flow ($z \gtrsim 0.01$) are used to measure H_0 due to to their high precision (5% in distance per source) and high luminosity which allows deep reach and thus reduces the impact of local velocity flows.

Table 1. A comparison of the latest SH0ES data release (R21) with previous data updates.

SH0ES Year/Ref.	Cepheid + SnIa Host Galaxies	Cepheids		Calibrator SnIa	Hubble Flow SnIa
2016 R16 [153]	19 $z < 0.01$	MW	15	19 $z < 0.01$	217 $0.0233 < z < 0.15$
		LMC [a]	785		
		N4258	139		
		M31	372		
		Total	1311		
		In SnIa hosts	975		
		Total All	2286		
2019 R19 [154]	19 $z < 0.01$	MW	15	19 $z < 0.01$	217 $0.0233 < z < 0.15$
		LMC [b]	785 + 70		
		N4258	139		
		M31	372		
		Total	1381		
		In SnIa hosts	975		
		Total All	2356		
2020 R20 [155]	19 $z < 0.01$	MW	75	19 $z < 0.01$	217 $0.0233 < z < 0.15$
		LMC [b]	785 + 70		
		N4258	139		
		M31	372		
		Total	1441		
		In SnIa hosts	975		
		Total All	2416		
2021 R21 [1]	37 $0.0015 \lesssim z < 0.011$	LMC [b]	270 + 69	42 $0.0015 \lesssim z < 0.011$ (77 lightcurve meas.)	277 $0.023 < z < 0.15$
		SMC [a]	143		
		N4258	443		
		M31	55		
		Total	980		
		In SnIa hosts	2150		
		Total All	3130		

NOTE: (a) From the ground. (b) From the ground + HST.

The new SH0ES data release includes a factor of 3 increase in the sample of Cepheids within NGC 4258. In total it has 2150 Cepheids in SnIa hosts[3], 980 Cepheids in anchors or supporting galaxies[4], 42 SnIa (with total 77 lightcurve dataset measurements) in 37 Cepheid+SnIa hosts with redshifts $0.0015 \lesssim z < 0.011$ and 277 SnIa in the Hubble flow in the redshift range $0.023 < z < 0.15$. In addition 8 anchor based constraints (with uncertainties included) constrain the following Cepheid modeling parameters: M_W (the Cepheid absolute magnitude zeropoint), b_W (the slope of the Cepheid Period-Luminosity P-L relation), Z_W (the slope of the Cepheid Metallicity-Luminosity M-L relation), a zeropoint parameter zp used to refine the Cepheid P-L relation by describing the difference between the ground and HST zeropoints in LMC Cepheids (zp is set to 0 for HST observations), the distance moduli of the anchors NGC 4258 and LMC and a dummy parameter we call X which has been included in the R21 data release and is set to 0 with uncertainty 10^{-9}[5].

The parameters that fit with these data include the four modeling parameters M_W, b_W, Z_W, M_B (the SnIa absolute magnitude), the 37 distance moduli of SnIa/Cepheid hosts, the distance moduli to the 2 anchors (NGC 4258, LMC) and to the supporting Cepheid host M31, the zeropoint zp of the Cepheid P-L relation in the LMC ground observations, the Hubble parameter, and the dummy parameter mentioned above (tightly constrained to 0). This is a total of 47 parameters (46 if the dummy parameter X is ignored).

In addition to these parameters, there are other modeling parameters such as the color and shape correction slopes of SnIa (usually denoted as β and α) as well as the Wesenheit dust extinction parameter R_W, which were incorporated in the released SnIa and Cepheid apparent magnitudes and thus cannot be used as independent parameters in the analysis, in contrast to the previous data release.

The provided R21 Cepheid Wesenheit dust-corrected dereddened apparent magnitudes m_H^W are connected with the Wesenheit dust extinction parameter R_W as [158] (see also Refs. [153,154])

$$m_H^W \equiv m_H - R_W(V - I) \tag{4}$$

where m_H is the observed apparent magnitude in the near-infrared H (F160W) band, and V (F555W) and I (F814W) are the optical mean apparent magnitudes in the corresponding bands. The empirical parameter R_W is also called 'the reddening-free "Wesenheit" color ratio' and is different from R_H, which can be derived from a dust law (e.g., the Fitzpatrick law [159]). The parameter R_W corrects for both dust and intrinsic variations applied to observed blackbody colors $V - I$.

The provided in R21 SnIa apparent magnitudes m_B^0, standardized using light curve color c and shape x_1 corrections, are defined as

$$m_B^0 \equiv m_B - \alpha\, x_1 - \beta\, c = \mu + M_B \tag{5}$$

where m_B is the peak apparent magnitude, μ is the SnIa distance modulus, while the B-band absolute magnitude, M_B, and correction coefficients α and β are fit directly using the SnIa data. The latest SH0ES data release provides the measured values of m_H^W and m_B^0 for Cepheid and SnIa, respectively, which are also used in the corresponding analysis, while the parameters R_W, α and β were fit previously and independently by the SH0ES team to provide the values of m_H^W and m_B^0.

1.3. The Prospect of New Degrees of Freedom in the SH0ES Data Analysis

The homogeneity of the SH0ES data with respect to the parameters R_W, α and β were analyzed in previous studies with some interesting results. In particular, using the data of the previous SH0ES data release [153–155], it was shown [146] (see also [113] for a relevant study) that if the parameter R_W is allowed to vary among Cepheid and SnIa hosts, then the fit quality is significantly improved, and the best-fit value of H_0 is lowered to a level consistent with the inverse distance ladder best fit. In addition, a more recent analysis allowed the parameter β to have a different value in Hubble flow SnIa ($\beta = \beta_{HF}$ for $z > 0.02$) compared to calibrating SnIa ($\beta = \beta_{cal}$ for $z < 0.01$). A reanalysis allowing for this new degree of freedom indicated a tension between the the two best-fit values (β_{HF} and β_{cal}) at a level of up to 3.8σ [117].

Motivated by these hints for inhomogeneities in the SH0ES data, in what follows, we introduce new degrees of freedom in the analysis that are designed to probe the origin of these inhomogeneities. We thus accept three of the four above-mentioned assumptions that have led to the Hubble tension and test the validity of the fourth assumption. In particular, we keep the following assumptions:

1. There are no significant systematics in the SH0ES data, and thus they are reliable.
2. The CMB sound horizon scale used as a calibrator in the inverse distance ladder approach is correctly obtained in the standard model using the known particles.
3. The Hubble expansion history from the time of recombination up to $z = 0.01$ (or even $z = 0$) used in the inverse distance ladder measurement of H_0 is provided correctly by the standard Planck18/ΛCDM cosmological model.

As discussed above, there are several studies in the literature that support the validity of these assumptions (e.g., [45,104]). If these assumptions are valid, then the most probable source of the Hubble tension is the violation of the fourth assumption stated above, namely *'the physical laws involved and the calibration properties of Cepheids and SnIa in all the rungs of the distance ladder are well understood and modeled properly'*.

If this assumption is violated, then the modeling of Cepheids+SnIa should be modified to take into account possible changes of physics by introducing new degrees of freedom that were suppressed in the original (baseline) SH0ES analysis. In the context of this approach, if these degrees of freedom are properly introduced in the analysis, then the

best-fit value of H_0 will become consistent with the corresponding inverse distance ladder value of $H_0 = 67.36 \pm 0.54$ km s^{-1} Mpc^{-1}.

In an effort to pursue this approach for the resolution of the Hubble tension, we address the following questions:

- How can new degrees of freedom (new parameters) be included in the SH0ES data analysis for the determination of H_0?
- What are the new degrees of freedom that can expose internal tensions and inhomogeneities in the Cepheid/SnIa data?
- What new degrees of freedom can lead to a best-fit value of H_0 that is consistent with Planck?

The main goal of the present analysis is to address these questions. The new degree of freedom we allow and investigate is a transition of any one of the four Cepheid/SnIa modeling parameters at a specific distance D_c or equivalently (in the context of the cosmological principle) at a given cosmic time t_c such that $t_0 - t_c = D_c/c$, where t_0 is the present cosmic time (age of the universe). In the context of this new degree of freedom, we reanalyze the SH0ES data to find how the quality of fit to the data and the best-fit value of H_0 change when the new degree of freedom is excited. The possible introduction of new constraints included in the analysis is also considered.

The structure of this paper is the following: in the next Section 2, we describe the standard analysis of the SH0ES Cepheid+SnIa data in a detailed and comprehensive manner, stressing some details of the released dataset that are not described in R21. We also describe some tension between the values of the best-fit Cepheid modeling parameters b_W and Z_W obtained in anchor or pure Cepheid host galaxies and the corresponding mean values obtained in SnIa host galaxies. In Section 3, we present our generalized analysis with new degrees of freedom that allow a transition of the main modeling parameters at specific distances (cosmic times of radiation emission). We also investigate the effect of the inverse distance ladder constraint on M_B [149,160,161] for both the baseline SH0ES analysis and for our analysis involving the M_B transition degree of freedom. Finally, in Section 4, we conclude and discuss the implications of our results and the possible extensions of our analysis.

2. The New SH0ES Data and Their Standard Analysis: Hints for Intrinsic Tensions

2.1. The Original Baseline SH0ES Analysis: A Comprehensive Presentation

The main equations used to model the Cepheid SnIa measured apparent magnitudes with parameters that include H_0 are described as follows:

- The equation that connects the measured Wesenheit magnitude of the jth Cepheid in the ith galaxy with the host distance moduli μ_i and the modeling parameters M_W, b_W and Z_W is of the following form[6]

$$m^W_{H,i,j} = \mu_i + M^W_H + b_W[P]_{i,j} + Z_W[O/H]_{i,j} \quad (6)$$

where μ_i is the inferred distance modulus to the galaxy, M^W_H is the zeropoint Cepheid absolute magnitude of a period $P = 10\,d$ Cepheid (d for days), and $b_W - Z_W$ are the slope parameters that represent the dependence of magnitude on both period and metallicity. The $[O/H]$ is a measure of the metallicity of the Cepheid. The usual bracket shorthand notation for the metallicity $[O/H]$ represents the Cepheid metal abundance compared to that of the Sun

$$[O/H] \equiv \log(O/H) - \log(O/H)_\odot = \Delta \log(O/H) \quad (7)$$

Here, O and H are the number of oxygen and hydrogen atoms per unit of volume, respectively. The unit often used for metallicity is the dex (decimal exponent) defined

as $n\,dex \equiv 10^n$. Additionally, the bracket shorthand notation for the period $[P]$ is used as (P in units of days)

$$[P] \equiv \log P - 1 \tag{8}$$

- The color- and shape-corrected SnIa B-band peak magnitude in the ith host is connected with the distance modulus μ_i of the ith host and with the SnIa absolute magnitude M_B as shown in Equation (5), i.e.,

$$m^0_{B,i} = \mu_i + M_B \tag{9}$$

The distance modulus is connected with the luminosity distance d_L in Mpc as

$$\mu = 5\log(d_L/Mpc) + 25 \tag{10}$$

where in a flat universe

$$d_L(z) = c(1+z)\int_0^z \frac{dz'}{H(z')} = cH_0^{-1}(1+z)\int_0^z \frac{H_0\,dz'}{H(z')} \equiv H_0^{-1}\,D_L(z) \tag{11}$$

where $D_L(z)$ is the Hubble free luminosity distance, which is independent of H_0.

- Using Equations (9)–(11), it is easy to show that that H_0 is connected with the SnIa absolute magnitude and the Hubble free luminosity distance as

$$5\log H_0 = M_B + 5\log D_L(z) - m^0_B(z) + 25 \tag{12}$$

In the context of the cosmographic expansion of $H(z)$ valid for $z << 1$, we have

$$\log D_L(z)_c \simeq \log\left[cz\left(1 + \frac{1}{2}(1-q_0)z - \frac{1}{6}(1-q_0-3q_0^2+j_0)z^2 + \mathcal{O}(z^3)\right)\right] \tag{13}$$

where $q_0 \equiv -\frac{1}{H_0^2}\frac{d^2a(t)}{dt^2}\Big|_{t=t_0}$ and $j_0 \equiv \frac{1}{H_0^3}\frac{d^3a(t)}{dt^3}\Big|_{t=t_0}$ are the deceleration and jerk parameters, respectively. Thus, Equations (12) and (13) lead to the equation that connects H_0 with the SnIa absolute magnitude M_B, which may be expressed as

$$5\log H_0 = M_B + 5\log D_L(z) - m^0_B(z) + 25 \equiv M_B + 5\,a_B + 25 \tag{14}$$

where we have introduced the parameter $a_B \equiv \log D_L(z) - 0.2m^0_B(z)$ as defined in the SH0ES analysis [153].

Thus, the basic modeling equations used in the SH0ES analysis for the measurement of H_0 are Equations (6), (9) and (14). In these equations, the input data are the measured apparent magnitudes (luminosities) of Cepheids $m^W_{H,i,j}$ and the SnIa apparent magnitudes $m^0_{B,i}$ (in Cepheid+SnIa hosts and in the Hubble flow). The parameters to be fit using a maximum likelihood method are the distance moduli μ_i (of the anchors and supporting hosts, the Cepheid+SnIa hosts and Hubble flow SnIa), the four modeling parameters (M^W_H, b_W, Z_W and M_B), the Hubble constant H_0, the zeropoint zp of the Cepheid P-L relation in the LMC ground measurements and the dummy parameter X. This is a total of 47 parameters. The actual data were released by the SH0ES team as a .fits file in the form of a column vector Y with 3492 entries, which include 8 constraints on the parameters obtained from measurements in anchor galaxies where the distance moduli are measured directly with geometric methods.

The entries of the provided Y data column vector do not include the pure measured apparent magnitudes. Instead, its entries are residuals defined by subtracting specific quantities. In particular, we have the following:

- The Cepheid Wesenheit magnitudes are presented as residuals with respect to a fiducial P-L term as

$$\bar{m}^W_{H,i,j} \equiv m^W_{H,i,j} - b^0_W[P] \tag{15}$$

  where $b^0_W = -3.286$ is a fiducial Cepheid P-L slope. As a result of this definition, the derived best-fit slope is actually a residual slope $\Delta b_W \equiv b_W - b^0_W$.
- The residual Cepheid Wesenheit magnitudes of the Cepheids in the anchors N4258, LMC and the supporting pure Cepheid host SMC (non SnIa hosts), are presented after subtracting a corresponding fiducial distance modulus obtained with geometric methods[7].
- The SnIa standardized apparent magnitudes in the Hubble flow are presented as residuals after subtracting the Hubble free luminosity distance with cosmographic expansion $5\log D_L(z)_c + 25$ (see Equation (13)).

Thus, the released data vector Y has the following form

$$\mathbf{Y} = \begin{pmatrix} \bar{m}^W_{H,1} \\ \dots \\ \bar{m}^W_{H,2150} \\ \hline \bar{m}^W_{H,N4258,1} - \mu_{0,N4258} \\ \dots \\ \bar{m}^W_{H,N4258,443} - \mu_{0,N4258} \\ \bar{m}^W_{H,M31,1} \\ \dots \\ \bar{m}^W_{H,M31,55} \\ \bar{m}^W_{H,LMC,ground,1} - \mu_{0,LMC} \\ \dots \\ \bar{m}^W_{H,LMC,ground,270} - \mu_{0,LMC} \\ \bar{m}^W_{H,SMC,ground,1} - \mu_{0,SMC} \\ \dots \\ \bar{m}^W_{H,SMC,ground,143} - \mu_{0,SMC} \\ \bar{m}^W_{H,LMC,HST,1} - \mu_{0,LMC} \\ \dots \\ \bar{m}^W_{H,LMC,HST,69} - \mu_{0,LMC} \\ \hline \bar{m}^0_{B,1} \\ \dots \\ m^0_{B,77} \\ \hline -5.803\ (M^W_{H,HST}) \\ -5.903\ (M^W_{H,Gaia}) \\ -0.21\ (Z_{W,Gaia}) \\ 0\ (X) \\ 0\ (\Delta zp) \\ 0\ (\Delta b_W) \\ 0\ (\Delta \mu_{N4258}) \\ 0\ (\Delta \mu_{LMC}) \\ \hline m^0_{B,1} - 5\log[cz_1(...)] - 25 \\ \dots \\ m^0_{B,277} - 5\log[cz_{277}(...)] - 25 \end{pmatrix}$$

} 2150 *Cepheids in 37 SnIa hosts*

} 980 *Cepheids in non SnIa hosts*

} *77 SnIa in Cepheid hosts*

} 8 *External constraints*

} 277 *SnIa in Hubble flow*

The eight external anchor constraints on the parameters that appear in this vector are the following:

$$\begin{aligned} M_H^W &= -5.803 \pm 0.082 \\ M_H^W &= -5.903 \pm 0.025 \\ Z_W &= -0.21 \pm 0.12 \\ X &= 0 \pm 0.00003 \\ \Delta zp &= 0 \pm 0.1 \\ \Delta b_W &= 0 \pm 10 \\ \Delta\mu_{N4258} &= 0 \pm 0.03 \\ \Delta\mu_{LMC} &= 0 \pm 0.026 \end{aligned} \tag{16}$$

The parameters to be fit using the Y vector data may also be expressed as a vector q with 47 entries of the following form

$$\mathbf{q} = \left.\begin{pmatrix} \mu_1 \\ \cdots \\ \mu_{37} \\ \Delta\mu_{N4258} \\ M_H^W \\ \Delta\mu_{LMC} \\ \mu_{M31} \\ \Delta b_W \\ M_B \\ Z_W \\ X \\ \Delta zp \\ 5\log H_0 \end{pmatrix}\right\} 47 \text{ parameters}$$

Using the column vectors **Y** and **q**, Equations (6), (9) and (14) and the constraints stated above can be expressed in matrix multiplication form as

$$\mathbf{Y} = \mathbf{Lq} \tag{17}$$

with **Y**, the matrix of measurements (data vector), **q**, the matrix of parameters and **L**, a model (or design) matrix which has 3492 rows corresponding to the entries of the **Y** data vector and 47 columns corresponding to the entries of the parameter vector **q**. The model matrix **L** also includes some data (Cepheid period and metallicity), and in the context of this baseline, the modeling of data has the form

$$
\mathbf{L} = \left(\begin{array}{cccccccccccccc}
1 & \dots & 0 & 0 & 1 & 0 & 0 & [P]_1 & 0 & [O/H]_1 & 0 & 0 & 0 \\
\dots & \dots & \dots & \dots & \dots & \dots & \dots & \dots & \dots & \dots & \dots & \dots & \dots \\
0 & \dots & 1 & 0 & 1 & 0 & 0 & [P]_{2150} & 0 & [O/H]_{2150} & 0 & 0 & 0 \\
\hline
0 & \dots & 0 & 1 & 1 & 0 & 0 & [P]_{N4258,1} & 0 & [O/H]_{N4258,1} & 0 & 0 & 0 \\
\dots & \dots & \dots & \dots & \dots & \dots & \dots & \dots & \dots & \dots & \dots & \dots & \dots \\
0 & \dots & 0 & 1 & 1 & 0 & 0 & [P]_{N4258,443} & 0 & [O/H]_{N4258,443} & 0 & 0 & 0 \\
0 & \dots & 0 & 0 & 1 & 0 & 1 & [P]_{M31,1} & 0 & [O/H]_{M31,1} & 0 & 0 & 0 \\
\dots & \dots & \dots & \dots & \dots & \dots & \dots & \dots & \dots & \dots & \dots & \dots & \dots \\
0 & \dots & 0 & 0 & 1 & 0 & 1 & [P]_{M31,55} & 0 & [O/H]_{M31,55} & 0 & 0 & 0 \\
0 & \dots & 0 & 0 & 1 & 1 & 0 & [P]_{LMC,ground,1} & 0 & [O/H]_{LMC,ground,1} & 0 & 1 & 0 \\
\dots & \dots & \dots & \dots & \dots & \dots & \dots & \dots & \dots & \dots & \dots & \dots & \dots \\
0 & \dots & 0 & 0 & 1 & 1 & 0 & [P]_{LMC,ground,270} & 0 & [O/H]_{LMC,ground,270} & 0 & 1 & 0 \\
0 & \dots & 0 & 0 & 1 & 1 & 0 & [P]_{SMC,ground,1} & 0 & [O/H]_{SMC,ground,1} & 0 & 1 & 0 \\
\dots & \dots & \dots & \dots & \dots & \dots & \dots & \dots & \dots & \dots & \dots & \dots & \dots \\
0 & \dots & 0 & 0 & 1 & 1 & 0 & [P]_{SMC,ground,143} & 0 & [O/H]_{SMC,ground,143} & 0 & 1 & 0 \\
0 & \dots & 0 & 0 & 1 & 1 & 0 & [P]_{LMC,HST,1} & 0 & [O/H]_{LMC,HST,1} & 0 & 0 & 0 \\
\dots & \dots & \dots & \dots & \dots & \dots & \dots & \dots & \dots & \dots & \dots & \dots & \dots \\
0 & \dots & 0 & 0 & 1 & 1 & 0 & [P]_{LMC,HST,69} & 0 & [O/H]_{LMC,HST,69} & 0 & 0 & 0 \\
\hline
1 & \dots & 0 & 0 & 0 & 0 & 0 & 0 & 1 & 0 & 0 & 0 & 0 \\
\dots & \dots & \dots & \dots & \dots & \dots & \dots & \dots & \dots & \dots & \dots & \dots & \dots \\
0 & \dots & 1 & 0 & 0 & 0 & 0 & 0 & 1 & 0 & 0 & 0 & 0 \\
\hline
0 & \dots & 0 & 0 & 1 & 0 & 0 & 0 & 0 & 0 & 0 & 0 & 0 \\
0 & \dots & 0 & 0 & 1 & 0 & 0 & 0 & 0 & 0 & 0 & 0 & 0 \\
0 & \dots & 0 & 0 & 0 & 0 & 0 & 0 & 0 & 1 & 0 & 0 & 0 \\
0 & \dots & 0 & 0 & 0 & 0 & 0 & 0 & 0 & 0 & 1 & 0 & 0 \\
0 & \dots & 0 & 0 & 0 & 0 & 0 & 0 & 0 & 0 & 0 & 1 & 0 \\
0 & \dots & 0 & 0 & 0 & 0 & 0 & 1 & 0 & 0 & 0 & 0 & 0 \\
0 & \dots & 0 & 1 & 0 & 0 & 0 & 0 & 0 & 0 & 0 & 0 & 0 \\
0 & \dots & 0 & 0 & 0 & 1 & 0 & 0 & 0 & 0 & 0 & 0 & 0 \\
\hline
0 & \dots & 0 & 0 & 0 & 0 & 0 & 0 & 1 & 0 & 0 & 0 & -1 \\
\dots & \dots & \dots & \dots & \dots & \dots & \dots & \dots & \dots & \dots & \dots & \dots & \dots \\
0 & \dots & 0 & 0 & 0 & 0 & 0 & 0 & 1 & 0 & 0 & 0 & -1
\end{array}\right)
$$

} 2150 *Cepheids in* 37 *SnIa hosts*

} 980 *Cepheids in non SnIa hosts*

} 77 *SnIa in Cepheid hosts*

} 8 *External constraints*

} 277 *SnIa in Hubble flow*

The system (17) has 3492 equations and 47 unknown parameter values. Thus, it is overdetermined and at best, it can be used in the context of the maximum likelihood analysis to find the best-fit parameter values that have maximum likelihood and thus minimum χ^2. For the definition of χ^2, the measurement error matrix (covariance matrix) $\mathbf{C}$ is needed and provided in the data release as a square matrix with dimension 3492×3492[8]. In Appendix A, we present the schematic form of the matrix $\mathbf{C}$, which also includes the standard uncertainties of the constraints as diagonal elements. Using the covariance matrix that quantifies the data uncertainties and their correlation, the χ^2 statistic may be constructed as

$$\chi^2 = (\mathbf{Y} - \mathbf{Lq})^{\mathbf{T}} \mathbf{C}^{-\mathbf{1}} (\mathbf{Y} - \mathbf{Lq}) \tag{18}$$

The numerical minimization of χ^2 in the presence of 47 parameters that need to be fit would be very computationally demanding, even with the use of Markov chain Monte Carlo (MCMC) methods. Fortunately, the linear form of the system (17) allows the analytical minimization of χ^2 and the simultaneous analytic evaluation of the uncertainty of each parameter. In Appendix B, we show that the analytic minimization of χ^2 of Equation (18) leads to the best-fit parameter maximum likelihood vector[9]

$$\mathbf{q_{best}} = (\mathbf{L}^{\mathbf{T}} \mathbf{C}^{-\mathbf{1}} \mathbf{L})^{-\mathbf{1}} \mathbf{L}^{\mathbf{T}} \mathbf{C}^{-\mathbf{1}} \mathbf{Y} \tag{19}$$

The 1σ standard errors for the parameters in $\mathbf{q_{best}}$ are obtained as the square roots of the 47 diagonal elements of the transformed error matrix

$$\Sigma = (\mathbf{L}^{\mathbf{T}} \mathbf{C}^{-\mathbf{1}} \mathbf{L})^{-\mathbf{1}} \tag{20}$$

For example the best fit of the parameter[10] $5 \log H_0$ is obtained as the 47th entry of the best fit parameter vector $\mathbf{q_{best}}$ and the corresponding 1σ standard error is the $\sqrt{\Sigma_{47,47}}$ element of the error matrix. Using equations (19) and (20) and the latest released data of the SH0ES team presented in R21 we find full agreement with all values of the best fit parameters. For example for H_0 we find (after implementing error propagation) $H_0 = 73.04 \pm 1.04$ km s^{-1} Mpc^{-1} fully in agreement with the published result of R21.

In Table 2, we show the best-fit values and uncertainties for all 47 parameters of the vector $\mathbf{q}$, including the four Cepheid modeling parameters ($b_W = b_W^0 + \Delta b_W \equiv -3.286 + \Delta b_W$, M_H^W, Z_W and M_B) along with the best-fit value of H_0 for the baseline SH0ES model. The corresponding best-fit values and uncertainties with an additional constraint on M_B from the inverse distance ladder are also included and discussed in detail in the next section. The agreement with the corresponding results of R21 (left three columns) is excellent.

Before closing this subsection, we review a few points that are not mentioned in R21 but are useful for the reproduction of the results and the analysis:

- The number of entries of the parameter vector $\mathbf{q}$ is 47 and not 46 as implied in R21 due to the extra dummy parameter X, which is included in the released data $\mathbf{Y}$, $\mathbf{L}$ and $\mathbf{C}$ but not mentioned in R21.
- The entry referred as b_W in R21 in the parameter vector $\mathbf{q}$ should be Δb_W because it is actually the residual b_W ($\Delta b_W \equiv b_W - b_W^0$) as stated above and not the original slope of the P-L relation (its best-fit value is $\Delta b_W = -0.014 \pm 0.015$).
- The number of constraints shown in the definition of the $\mathbf{Y}$ vector in R21 is five, while in the actual released data $\mathbf{Y}$, $\mathbf{L}$ and $\mathbf{C}$, we found the eight constraints defined above.

2.2. Homogeneity of the Cepheid Modeling Parameters

Before generalizing the model matrix $\mathbf{L}$ with new degrees of freedom and/or constraints, it is interesting to test the self-consistency of the assumed universal modeling parameters b_W and Z_W of the Cepheids. These parameters can be obtained separately for each one of the $i = 1, ..., 40$ Cepheid hosts[11] by fitting linear relations.

In particular, in order to obtain the best-fit P-L slope $b_{W,i}$ of the *ith* Cepheid host, we fit the $m_{H,i,j}^W - \log P_{i,j}$ data (where $P_{i,j}$ is the period in units of days of the *jth* Cepheid in the *ith* host) with a linear relation of the form

$$m_{H,i,j}^W = s_i + b_{W,i} \log P_{i,j} \tag{21}$$

with parameters to be fit in each host $s_i - b_{W,i}$ (intercept and slope). These equations may be expressed as a matrix equation of the form

$$\mathbf{Y_i} = \mathbf{A_i X_i} \tag{22}$$

with $\mathbf{Y_i}$ as the vector of measurements, $\mathbf{X_i}$ as the vector of parameters and $\mathbf{A_i}$ as the model (or design) matrix. These are defined as

$$\mathbf{Y_i} = \begin{pmatrix} m_{H,i,1}^W \\ m_{H,i,2}^W \\ \vdots \\ m_{H,i,N}^W \end{pmatrix} \quad , \quad \mathbf{X_i} = \begin{pmatrix} s_i \\ b_{W,i} \end{pmatrix} \quad , \quad \mathbf{A_i} = \begin{pmatrix} 1 & \log P_{i,1} \\ 1 & \log P_{i,2} \\ \vdots & \vdots \\ 1 & \log P_{i,N} \end{pmatrix} \tag{23}$$

The analytically (along the lines of the previous subsection and of Appendix B) obtained minimum of

$$\chi_i^2 = (\mathbf{Y_i} - \mathbf{A_i X_i})^{\mathbf{T}} \mathbf{C_i}^{-1} (\mathbf{Y_i} - \mathbf{A_i X_i}) \tag{24}$$

with respect to the slope $b_{W,i}$ and intercept s_i leads to the best-fit values and standard errors for these parameters. For all Cepheids, we adopt the N × N covariance matrix $\mathbf{C_i}$ of standard errors of the magnitude measurements from R21.

Thus, the analytic minimization of χ^2 of Equation (24) leads to the best-fit parameter maximum likelihood vector

$$\mathbf{X_{i,best}} = (\mathbf{A_I}^{\mathbf{T}} \mathbf{C_i}^{-1} \mathbf{X_i})^{-1} \mathbf{A_i}^{\mathbf{T}} \mathbf{C_i}^{-1} \mathbf{Y_i} \tag{25}$$

The 1σ standard errors for $b_{W,i}$ slope and intercept in $\mathbf{X_{i,best}}$ are obtained as the square roots of the two diagonal elements of the error matrix

$$\Sigma_\mathbf{i} = (\mathbf{A_i}^{\mathbf{T}} \mathbf{C_i}^{-1} \mathbf{A_i})^{-1} \tag{26}$$

A similar analysis was implemented for the other Cepheid modeling parameter, the metallicity slopes $Z_{W,i}$. In this case, the linear fit considered was of the form

$$m^W_{H,i,j} = s_i + Z_{W,i}[O/H]_{i,j} \tag{27}$$

The best-fit values of the slopes $b_{W,i}$ and $Z_{W,i}$ for each of the 40 Cepheid hosts are shown in Figures 1 and 2 in terms of the host distance, respectively. The actual Cepheid data in each host with the best-fit $\log P_{i,j} - m^W_{H,i,j}$ and $[O/H]_{i,j} - m^W_{H,i,j}$ straight lines are shown in Figures A2 and A3 in Appendix C for each of the 40 Cepheid hosts i. The $b_{W,i}$ slopes shown in Figure A4 for each host in sequence of increasing uncertainties, is in excellent agreement with the corresponding Figure 10 shown in R21[12]. The corresponding numerical values of the best fit $b_{W,i}$ and $Z_{W,i}$ are shown in Table A1.

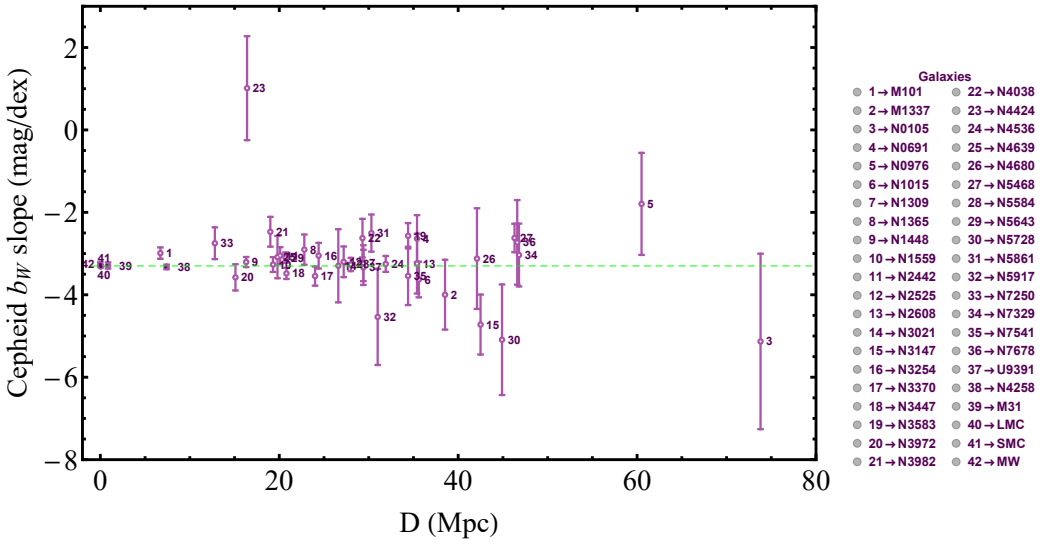

Figure 1. Independently fitted slopes $b_{W,i}$ of the Cepheid P-L relations. Here, we ignored non-diagonal terms of the covariance as was done in R21 in the corresponding Figure 10. There is a consistent trend of most non-anchor hosts having a best-fit absolute slope $|b_W|$ that is smaller than corresponding best fit b_W of the anchor hosts (above the dotted line). The dotted line corresponds to the best-fit value of $b_W = b_W^0 + \Delta b_W = -0.286 - 0.013 = -0.299$ in the context of the baseline SH0ES analysis as shown in Table 2.

Table 2. Best-fit parameter values in the absence and in the presence of the inverse distance ladder constraint for baseline model.

Parameter	Best Fit Value	σ	Best Fit Value [a]	σ [a]
μ_{M101}	29.16	0.04	29.20	0.04
μ_{M1337}	32.92	0.08	32.97	0.08
μ_{N0691}	32.82	0.09	32.87	0.09
μ_{N1015}	32.62	0.069	32.67	0.06
μ_{N0105}	34.49	0.12	34.56	0.12
μ_{N1309}	32.51	0.05	32.56	0.05
μ_{N1365}	31.33	0.05	31.37	0.05
μ_{N1448}	31.3	0.04	31.33	0.03
μ_{N1559}	31.46	0.05	31.51	0.05
μ_{N2442}	31.47	0.05	31.51	0.05
μ_{N2525}	32.01	0.06	32.08	0.06
μ_{N2608}	32.63	0.11	32.69	0.11
μ_{N3021}	32.39	0.1	32.45	0.1
μ_{N3147}	33.09	0.09	33.16	0.08
μ_{N3254}	32.4	0.06	32.46	0.05
μ_{N3370}	32.14	0.05	32.19	0.04
μ_{N3447}	31.94	0.03	31.98	0.03
μ_{N3583}	32.79	0.06	32.84	0.06
μ_{N3972}	31.71	0.07	31.76	0.07
μ_{N3982}	31.64	0.06	31.69	0.05
μ_{N4038}	31.63	0.08	31.69	0.08
μ_{N4424}	30.82	0.11	30.87	0.11
μ_{N4536}	30.84	0.05	30.87	0.05
μ_{N4639}	31.79	0.07	31.83	0.07
μ_{N4680}	32.55	0.15	32.61	0.15
μ_{N5468}	33.19	0.05	33.25	0.05
μ_{N5584}	31.87	0.05	31.91	0.04
μ_{N5643}	30.51	0.04	30.56	0.04
μ_{N5728}	32.92	0.1	32.98	0.1
μ_{N5861}	32.21	0.08	32.26	0.07
μ_{N5917}	32.34	0.08	32.4	0.08
μ_{N7250}	31.61	0.1	31.65	0.1
μ_{N7329}	33.27	0.07	33.33	0.07
μ_{N7541}	32.58	0.08	32.64	0.08
μ_{N7678}	33.27	0.08	33.33	0.08
μ_{N0976}	33.54	0.08	33.61	0.08
μ_{U9391}	32.82	0.05	32.86	0.05
$\Delta\mu_{N4258}$	-0.01	0.02	0.01	0.02
M_H^W	-5.89	0.02	-5.92	0.02
$\Delta\mu_{LMC}$	0.01	0.02	0.03	0.02
μ_{M31}	24.37	0.07	24.4	0.07
Δb_W	-0.013	0.015	-0.026	0.015
M_B	-19.25	0.03	-19.33	0.02
Z_W	-0.22	0.05	-0.22	0.05
X	0.	0.	0.	0.
Δzp	-0.07	0.01	-0.07	0.01
$5\log H_0$	9.32	0.03	9.24	0.02
H_0	73.04	1.04	70.5	0.7

NOTE: (a) With constraint $M_B = -19.401 \pm 0.027$ included in the data vector **Y** and in the model matrix **L** with included uncertainty in the extended covariance matrix **C**.

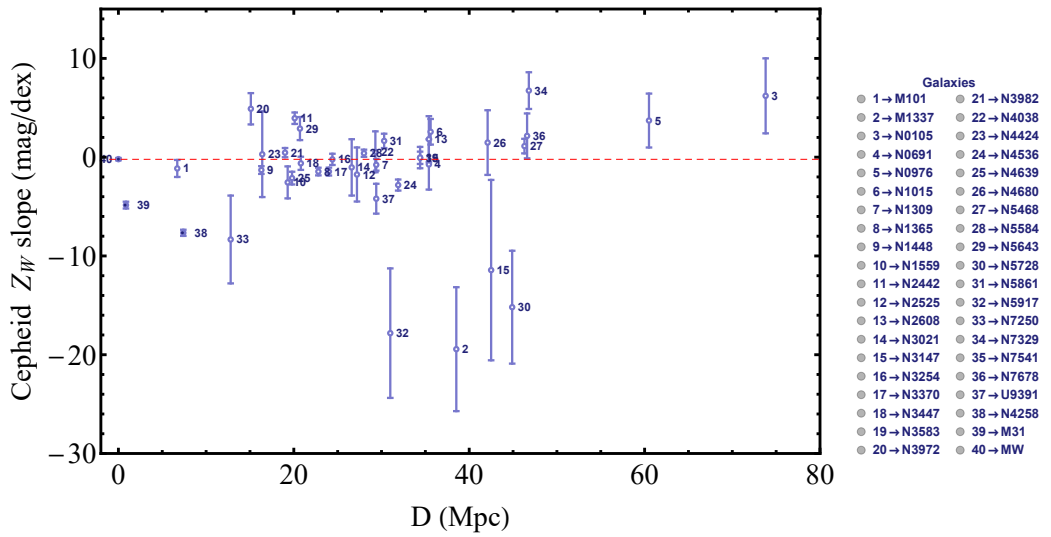

Figure 2. Independently fitted metallicity slopes $Z_{W,i}$ in terms of the distance of the Cepheid host. Clearly, the spread of many points is larger than the corresponding uncertainties indicating either inhomogeneities of the sample or underestimation of the uncertainties. In fact, there seems to be a trend of most $|Z_{W,i}|$ absolute slopes being larger than the corresponding slope of the Milky Way (MW) (below the dotted line). The dotted line corresponds to the best-fit value of $Z_W = -0.21$ in the context of the baseline SH0ES analysis as shown in Table 2.

Some inhomogeneities are visible in the distance distribution of both the individual Cepheid slopes in Figures 1 and 2 as well as in Figure A4. For example, in Figures 1 and A4, there is a consistent trend of most non-anchor hosts having an absolute best-fit slope b_W that is smaller than the corresponding best-fit b_W of the anchor hosts (above the dotted line). Similarly, in Figure 2, there seems to be a trend of most $Z_{W,i}$ absolute slopes being larger than the corresponding slope of the Milky Way (MW) (below the dotted line).

A careful inspection of Figures 1 and 2 indicates that the scatter is significantly larger than the standard uncertainties of the slopes. Indeed, a χ^2 fit to a universal slope for Z_W of the form

$$\chi^2(Z_W) = \sum_{i=1}^{N} \frac{(Z_{W,i} - Z_W)^2}{\sigma^2_{Z_{W,i}}} \tag{28}$$

leads to a minimum χ^2_{min} per degree of freedom (dof)[13] $\frac{\chi^2_{ZW,min}}{dof} = 22$ (with a best-fit $Z_{W,bf} \simeq -1$) while $\frac{\chi^2_{min}}{dof} = O(1)$ would be expected for an acceptable fit. Additionally, for b_W, we find $\frac{\chi^2_{bW,min}}{dof} = 1.55$ ($b_{W,bf} = -3.3$), which is more reasonable but still larger than 1, indicating a relatively poor quality of fit to a universal slope.

There are two possible causes for this poor quality of fit to universal slopes: either many of the uncertainties of the individual host slopes were underestimated, or the universal slope model is not appropriate. In view of the fact that the uncertainties of the Cepheid periods and metallicities are not included in the χ^2 fit because they were not provided by R21 released data, we make the working hypothesis that the uncertainties are underestimated, and thus we add a scatter error adjusted so that $\frac{\chi^2_{bW,min}}{dof} \simeq \frac{\chi^2_{ZW,min}}{dof} \simeq 1$. Thus for $\chi^2(Z_W)$, we have

$$\chi^2(Z_W) = \sum_{i=1}^{N} \frac{(Z_{W,i} - Z_W)^2}{\sigma^2_{Z_{W,i}} + \sigma^2_{Z,scat}} \tag{29}$$

For $\frac{\chi^2_{ZW,min}}{dof} \simeq 1$, we must set $\sigma_{Z,scat} \simeq 3.2$, which is significantly larger than most uncertainties of individual host Z_W slopes. Similarly, for $\frac{\chi^2_{bW,min}}{dof} \simeq 1$ we must set $\sigma_{b,scat} \simeq 0.18$, which is comparable to or smaller than most uncertainties of individual host b_W slopes as shown in Table A1.

In order to quantify possible inhomogeneities of Cepheid hosts $b_{W,i}$ and $Z_{W,i}$ slopes, we split each sample of slopes in two bins: a low-distance bin with Cepheid host distances D smaller than a critical distance D_c, and a high-distance bin with $D > D_c$. Given D_c, for each bin, we find the best-fit slope and its standard 1σ error using the maximum likelihood method. For example, for a low distance b_W bin, we minimize

$$\chi^2(b_W^<) = \sum_{i=1}^{N^<} \frac{(b_{W,i} - b_W^<)^2}{\sigma^2_{b_{W,i}} + \sigma^{2<}_{scat}} \tag{30}$$

where $N^<$ is the number of hosts in the low-distance bin and σ_{scat} is the additional uncertainty (scatter error) chosen in each bin so that $\chi^2 \simeq 1$ so that the fit becomes consistent with a constant b_W in each bin. Thus, we find the best-fit low-distance bin slope $b_W^<$ and its standard error and similarly for the high distance bin $D > D_c$, $b_W^>$ and for the slopes $Z_W^<$, $Z_W^>$. Thus for each D_c, we obtain two best-fit slopes (one for each bin) and their standard errors. The level of consistency between the two binned slopes at each D_c determines the level of homogeneity and self consistency of the full sample. The results for the best-fit binned slopes for b_W and Z_W are shown in Figures 3 and 4, respectively, as functions of the dividing critical distance D_c.

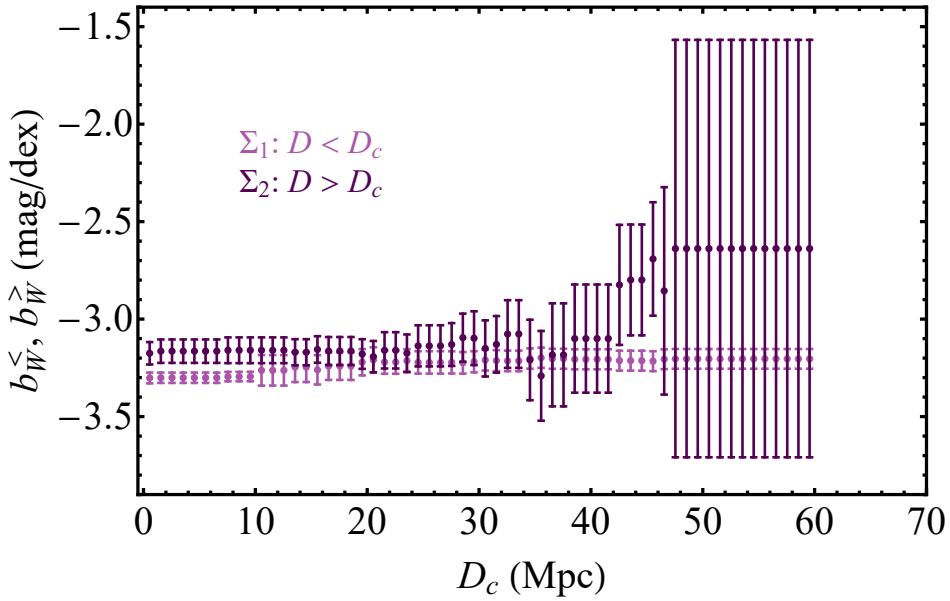

Figure 3. Binned Cepheid P-L slopes $b_W^>$ and $b_W^<$ for the high-distance bin Σ_2 ($D > D_c$) and the low distance bin Σ_1 ($D < D_c$), respectively. In each bin, σ_{scat} was used and adjusted so that $\chi^2_{bW,min} \simeq 1$. Notice that for $D_c \simeq 50$ Mpc, the high–low-distance bins are statistically consistent with each other due to small number of Cepheids in the high-distance bin, but the difference of their slope best-fit values is maximized.

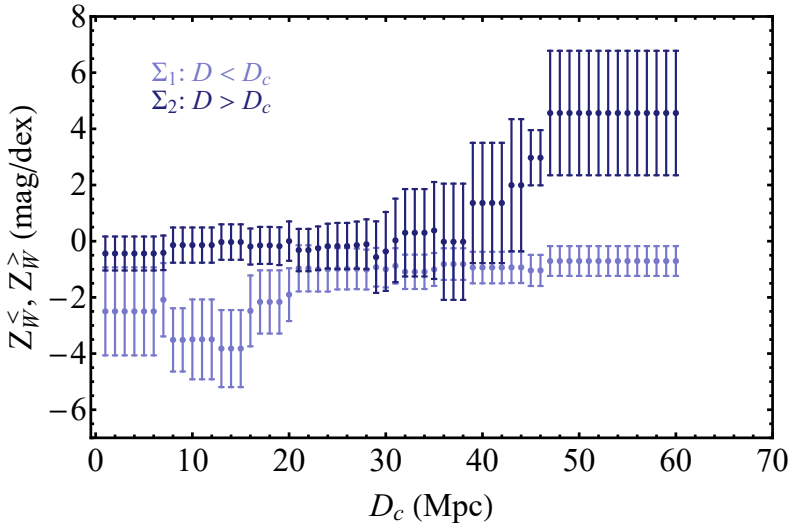

Figure 4. Binned Cepheid metallicity slopes $Z_W^>$ and $Z_W^<$ for the high-distance bin Σ_2 ($D > D_c$) and the low-distance bin Σ_1 ($D < D_c$), respectively. In each bin, the additional scattering uncertainty σ_{scat} was used and adjusted so that $\chi^2_{ZW,min} \simeq 1$. For $D_c \simeq 50$ Mpc, the difference between the best-fit bin slopes is maximized, and the tension between them is larger than 2σ (see also Figure 5).

Interestingly, for a range of D_c, there is a mild tension between the best-fit values of the high- and low-distance bins, which reaches levels of $2-3\sigma$, especially for the metallicity slopes Z_W. For both b_W and Z_W, the absolute value of the difference between the high- and low-distance bin slopes is maximized for $D_c > 47$ Mpc. For the case of Z_W, this difference is significant statistically, as it exceeds the level of 2σ. The level of statistical consistency between high- and low-distance bins for both slopes b_W and Z_W is shown in Figure 5. In the range of D_c between 40 Mpc and 50 Mpc and also between 10 Mpc and 20 Mpc, it is shown that in the case of Z_W, the σ-distance

$$\sigma_d \equiv \frac{|Z_W^> - Z_W^<|}{\sqrt{\sigma^2_{Z_W^>} + \sigma^2_{Z_W^<}}} \tag{31}$$

between the best-fit binned Z_W metallicity slopes can reach a level beyond 2σ (see Figures 4 and 5).

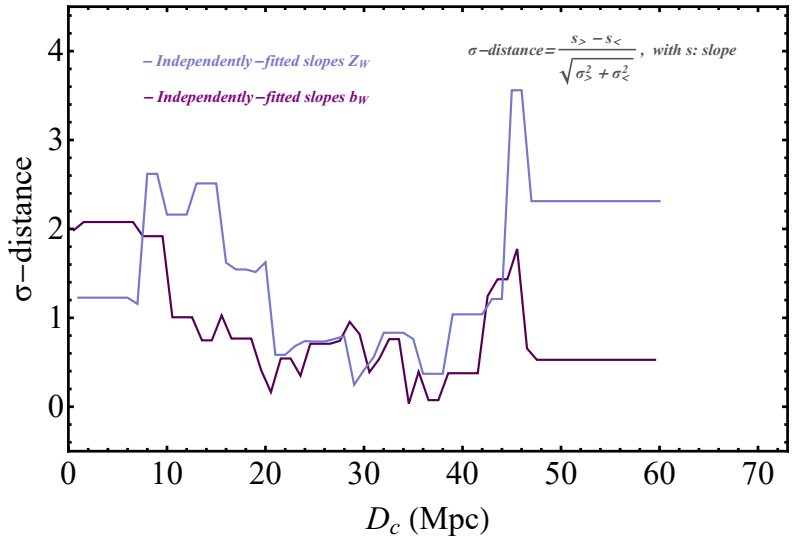

Figure 5. The σ distance between the best-fit high-distance bin ($D > D_c$) and low-distance bin slopes ($s^>(b_W^>, Z_W^>)$ and $s^<(b_W^<, Z_W^<)$) defined in Equation (31) for Z_W and similarly for b_W.

An additional test of possible intrinsic tensions of the Cepheid properties in the SH0ES Cepheid sample is obtained by comparing the probability distributions of the Cepheid period and metallicity for the full sample of the 3130 Cepheid with high- and low-distance subsamples. In Figures 6 and 7, we show histograms of the probability distributions of the Cepheid period and metallicity for the whole Cepheid sample and for the high- ($D > D_c$) and low-distance ($D < D_c$) subsamples for $D_c = 50$ Mpc. The two subsamples for each observable are clearly inconsistent with each other and with the full sample. This is demonstrated visually and also through the Kolmogorov–Smirnov consistency test, which quantifies the inconsistency and gives a p-value very close to 0 for the three sample pairs. However, as communicated to us by members of the SH0ES team (private communication), this inconsistency can be justified by observational selection effects and does not necessarily indicate a physics change at $D_c = 50$ Mpc. For example, bright Cepheids have longer periods and they are more easily observed at high distances. Thus, it is expected that there will be higher period (brighter) Cepheids observed at higher distances. Other variables, such as the time span of the observations, also play a role. For more distant galaxies, there is a trend to allow a longer window of observations so that longer period Cepheids can be found. Additionally, the star formation history of the galaxies dictates if one will have very long-period Cepheids which come from massive, short-lived stars. However, even though the observed inconsistency in the Cepheid properties probability distributions may be explained using observational biases and anticipated galactic properties, it may also be a hint of interesting new physics and/or systematic effects.

In view of the above level of mild inhomogeneities identified is the SH0ES data; it would be interesting to extend the SH0ES modeling of the Cepheids and SnIa with new degrees of freedom that can model the data, taking into account these inhomogeneities. This is the goal of the next section.

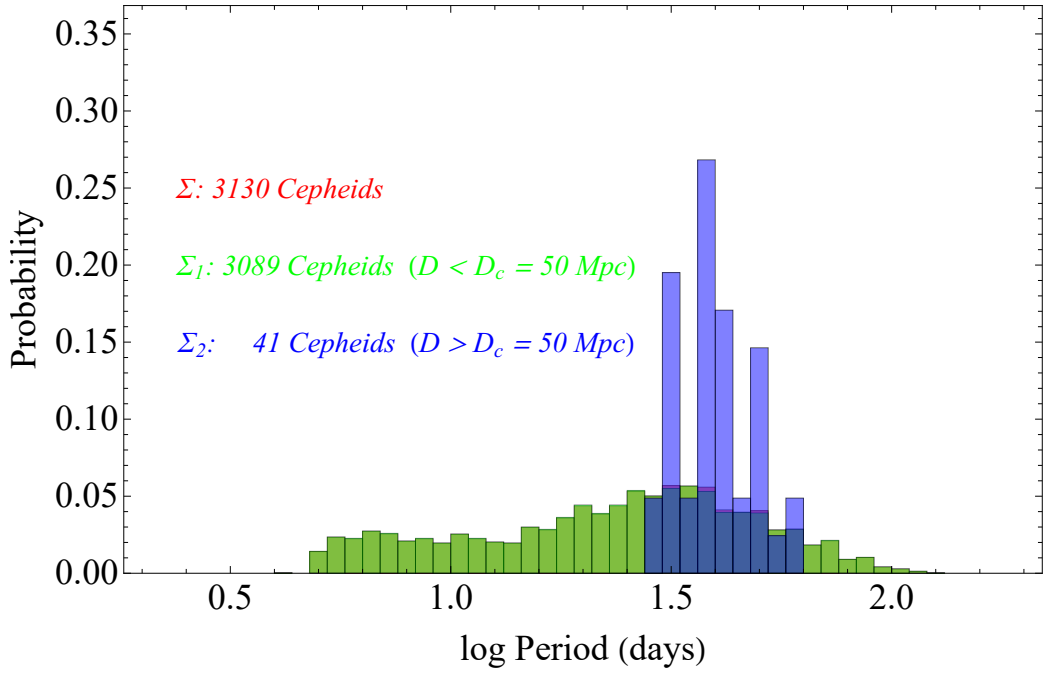

Figure 6. Probability distributions of the Cepheid period for the whole Cepheid sample and for the high ($D > D_c$) and low distance ($D < D_c$) subsamples for $D_c = 50$ Mpc. Due to the small number of Cepheids in the $D > 50$ Mpc bin (41), the probability distribution of the full sample (3130 Cepheids) is almost identical to the probability distribution of the $D < 50$ Mpc bin, and thus the light green bars overlap with the red bars.

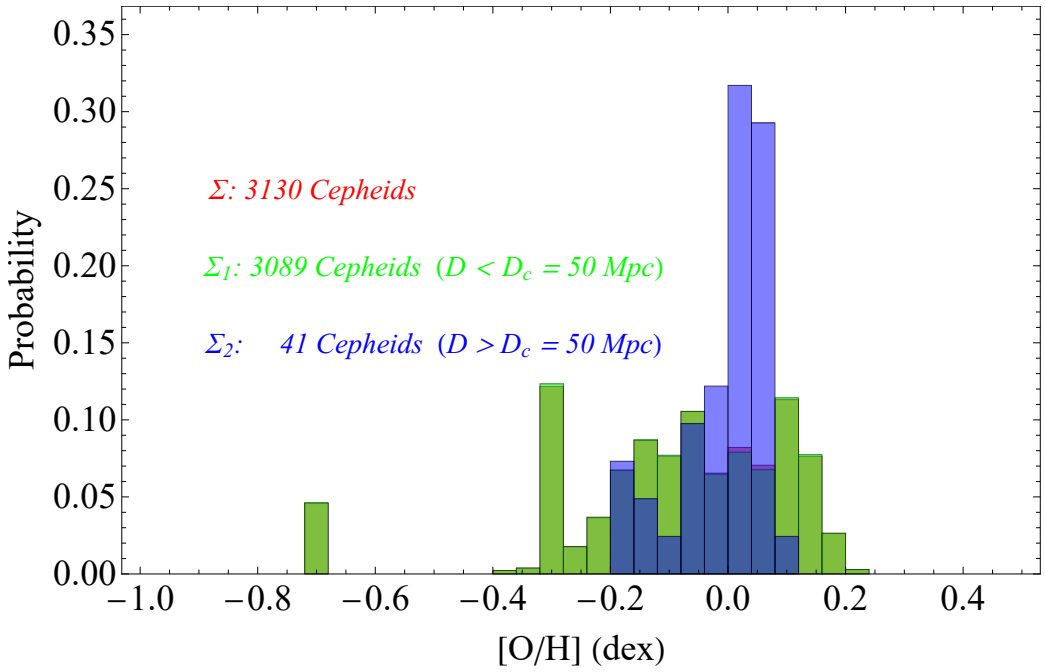

Figure 7. Probability distributions of the Cepheid metallicity for the whole Cepheid sample and for the high ($D > D_c$) and low distance ($D < D_c$) subsamples for $D_c = 50$ Mpc. Due to the small number of Cepheids in the $D > 50$ Mpc bin (41), the probability distribution of the full sample (3130 Cepheids) is almost identical to the probability distribution of the $D < 50$ Mpc bin, and thus the light green bars overlap with the red bars.

3. Generalized Analysis: New Degrees of Freedom Allowing for a Physics Transition

An obvious generalization of the SH0ES analysis described in Section 2.1 which models the Cepheid-SnIa luminosities using four main parameters is to allow for a transition of any one of these parameters at a particular distance or equivalently cosmic time when radiation is emitted. Such a transition could be either a result of a sudden change in a physics constant (e.g., the gravitational constant) during the last 200 Myrs in the context, e.g., of a first-order phase transition or a result of the presence of an unknown systematic.

Another modification of the standard SH0ES analysis in R21 would be to extend the number of constraints imposed on the data vector **Y** taking into account other cosmological data, such as the inverse distance ladder estimate of M_B [149,160,161]. Both of these generalizations will be implemented in the present section.

3.1. Allowing for a Transition of a Cepheid Calibration Parameter

A transition of one of the Cepheid calibration parameters can be implemented by replacing one of the four modeling parameters in the **q** vector by two corresponding parameters: one for high and one for low distances (recent cosmic times). Thus, in this approach, the number of parameters and entries in the parameter vector **q** increases by one, from 47 to 48. Since one of the entries of **q** is replaced by two entries, the corresponding column of the modeling matrix **L** should be replaced by two columns. The high distance parameter column should be similar to the original column it replaced, but with zeros in the entries, corresponding to low-distance data (or constraints), and the reverse should happen for the low-distance parameter column. This process is demonstrated in the following schematic diagram, where the q_j parameter is replaced by the two parameters q_j (or $q_j^<$) and q_{j+1} (or $q_j^>$), and the j column of **L** is replaced by the j and $j+1$ corresponding columns, which have zeros in the low- or high-distance data (or constraint) entries.

$$\mathbf{L}_{(\mathbf{3492}\times\mathbf{47})} = \left.\begin{pmatrix} \dots & L_{1,j} & \dots \\ \dots & L_{2,j} & \dots \\ \dots & L_{3,j} & \dots \\ \dots & \dots & \dots \\ \dots & \dots & \dots \\ \dots & L_{3491,j} & \dots \\ \dots & L_{3492,j} & \dots \end{pmatrix}\right\} \begin{matrix} D_{Y_1} < D_c \\ D_{Y_2} > D_c \\ D_{Y_3} > D_c \\ \dots \\ \dots \\ D_{Y_{3491}} < D_c \\ D_{Y_{3492}} > D_c \end{matrix} \Longrightarrow \mathbf{L}_{(\mathbf{3492}\times\mathbf{48})} = \begin{pmatrix} \dots & L_{1,j} & 0 & \dots \\ \dots & 0 & L_{2,j+1} & \dots \\ \dots & 0 & L_{3,j+1} & \dots \\ \dots & \dots & \dots & \dots \\ \dots & \dots & \dots & \dots \\ \dots & L_{3491,j} & 0 & \dots \\ \dots & 0 & L_{3492,j+1} & \dots \end{pmatrix} \quad (32)$$

$$\mathbf{q}_{(\mathbf{47}\times\mathbf{1})} = \begin{pmatrix} \dots \\ \dots \\ q_j \\ \dots \\ \dots \end{pmatrix} \rightarrow \mathbf{q}_{(\mathbf{48}\times\mathbf{1})} = \begin{pmatrix} \dots \\ \dots \\ q_j \\ q_{j+1} \\ \dots \\ \dots \end{pmatrix} \quad (33)$$

In this manner, if the parameter b_W was to be split to $b_W^>$ and $b_W^<$ for example, Equation (6) would be replaced by

$$m_{H,i,j}^W(D) = \mu_i + M_H^W + b_W^> \Theta(D - D_c)[P]_{i,j} + b_W^< \Theta(D_c - D)[P]_{i,j} + Z_W[O/H]_{i,j} \quad (34)$$

and similarly for splittings of each of the other three parameters, M_H^W, Z_W and M_B. In (34), D is a distance that may be assigned to every entry of the data vector $\mathbf{Y}$ (Cepheids, SnIa and constraints). Notice that the splitting of any parameter to high- and low-distance versions does not affect the form of the $\mathbf{Y}$ data vector and the covariance matrix $\mathbf{C}$ of the data. In order to properly place the 0 entries of each one of the new columns, a distance must be assigned to every entry of $\mathbf{Y}$. We specified this distance for each host using the literature resources or the best-fit distance moduli of each host. These distances along with other useful properties of the Cepheids used in our analysis are shown in Table 3.

We thus considered four generalizations of the baseline SH0ES analysis, each one corresponding to a high–low-distance split of each of the four modeling parameters. For each generalization, we obtained the best-fit values and uncertainties of all 48 parameters of the generalized parameter vector $\mathbf{q}$ for several values of the critical distance $D_c \in [1, 60Mpc]$, which defined in each case the high–low-distance data bins. The best-fit values with uncertainties for the high–low D split parameter (green and blue points) and for H_0 (red points), for each generalization considered, is shown in Figures 8–11 in terms of D_c. Dotted lines correspond to the SH0ES R21 H_0 best fit and to the Planck18/ΛCDM best fit for H_0. The following comments can be made based on the results of Figures 8–11.

Table 3. Properties of the Cepheid hosts considered in the analysis.

Galaxy	SnIa	Ranking in Figure A4	Ranking in Table 3 in R21	Ranking in Data Vector Y	D [a] $[Mpc]$	Number of Fitted Cepheids	Initial Point in Vector Y	Final Point in Vector Y
M101	2011fe	8	1	1	6.71	259	1	259
M1337	2006D	34	2	2	38.53	15	260	274
N0691	2005W	28	4	3	35.4	28	275	302
N1015	2009ig	24	6	4	35.6	18	303	320
N0105	2007A	42	3	5	73.8	8	321	328
N1309	2002fk	25	7	6	29.4	53	329	381
N1365	2012fr	20	8	7	22.8	46	382	427
N1448	2001el,2021pit	7	9	8	16.3	73	428	500
N1559	2005df	11	10	9	19.3	110	501	610
N2442	2015F	13	11	10	20.1	177	611	787
N2525	2018gv	21	12	11	27.2	73	788	860
N2608	2001bg	31	13	12	35.4	22	861	882
N3021	1995al	35	14	13	26.6	16	883	898
N3147	1997bq,2008fv,2021hpr	32	15	14	42.5	27	899	925
N3254	2019np	16	16	15	24.4	48	926	973
N3370	1994ae	14	17	16	24	73	974	1046
N3447	2012ht	9	18	17	20.8	101	1047	1147
N3583	2015so	15	19	18	34.4	54	1148	1201
N3972	2011by	17	20	19	15.1	52	1202	1253
N3982	1998aq	19	21	20	19	27	1254	1280
N4038	2007sr	29	22	21	29.3	29	1281	1309
N4424	2012cg	40	23	22	16.4	9	1310	1318
N4536	1981B	12	24	23	31.9	40	1319	1358
N4639	1990N	27	25	24	19.8	30	1359	1388
N4680	1997bp	38	26	25	42.1	11	1389	1399
N5468	1999cp,2002cr	18	27	26	46.3	93	1400	1492
N5584	2007af	10	28	27	28	165	1493	1657
N5643	2013aa,2017cbv	6	29	28	20.7	251	1658	1908
N5728	2009Y	41	30	29	44.9	20	1909	1928
N5861	2017erp	26	31	30	30.3	41	1929	1969
N5917	2005cf	37	32	31	31	14	1970	1983
N7250	2013dy	22	33	32	12.8	21	1984	2004
N7329	2006bh	33	34	33	46.8	31	2005	2035
N7541	1998dh	30	35	34	34.4	33	2036	2068
N7678	2002dp	36	36	35	46.6	16	2069	2084
N0976	1999dq	39	5	36	60.5	33	2085	2117
U9391	2003du	23	37	37	29.4	33	2118	2150
Total						2150	1	2150
N4258	Anchor	4	38	38	7.4	443	2151	2593
M31	Supporting	5	39	39	0.86	55	2594	2648
LMC [b]	Anchor	2	40	40	0.05	270	2649	2918
SMC [b]	Supporting	3	41	41	0.06	143	2919	3061
LMC [c]	Anchor	2	40	42	0.05	69	3062	3130
Total						980	2151	3130
Total All						3130	1	3130

Note: (a) Distances from NASA/IPAC Extragalactic Database (https://ned.ipac.caltech.edu/, (accessed on 8 June 2022)). (b) From the ground. (c) From HST.

- When the SnIa absolute magnitude M_B is allowed to change at D_c (M_B transition) and for $D_c > 47Mpc$, the best-fit value of H_0 drops spontaneously to the best-fit Planck18/ΛCDM value, albeit with larger uncertainty 67.33 ± 4.65 (see Figure 8 and second row of Table 4). This remarkable result appears with no prior or other information from the inverse distance ladder results. Clearly, there are increased uncertainties of the best-fit parameter values for this range of D_c because the most distant usable Cepheid hosts are at distances 46.8 Mpc (N7329), 60.5 Mpc (N0976) and 73.8 Mpc (N0105) and only two of them are at distance beyond 47 Mpc. These hosts (N0975 and N0105) have a total of 41 Cepheids and 4 SnIa. Due to the large uncertainties involved, there is a neutral model preference for this transition degree of freedom at $D_c > 47$ Mpc (the small drop of χ^2 by $\Delta\chi^2 \simeq -1.5$ is balanced by the

additional parameter of the model). This, however, changes dramatically if the inverse distance ladder constraint on M_B is included in the vector **Y** as discussed below.

- For all four modeling parameters considered, there is a sharp increase in the absolute difference between the high–low-distance best-fit parameter values for $D_c \gtrsim 47$ Mpc. The statistical significance of this split, however, is low due to the relatively small number of available Cepheids at $D > 47$ Mpc.
- The best-fit value of H_0 changes significantly when the SnIa absolute magnitude M_B is allowed to make a transition at $D_c > 47$ Mpc but is not significantly affected if the three Cepheid modeling parameters M_W, b_W and Z_W are allowed to make a transition at any distance. This is probably due to the large uncertainties involved and due to the fact that H_0 is only indirectly connected with the three Cepheid modeling parameters.
- Each one of the transition degrees of freedom mildly reduces χ^2, thus improving the fit to the data, but these transition models are not strongly preferred by the model selection criteria, which penalize the extra parameter implied by these models. This is demonstrated in Figures 12 and 13, which show the values of $\Delta\chi^2_{min}$, ΔAIC and ΔBIC of the four transition models with respect to the baseline SH0ES model for various D_c transition distances. As discussed below, this changes dramatically if the inverse distance ladder constraint on M_B is introduced in the analysis.

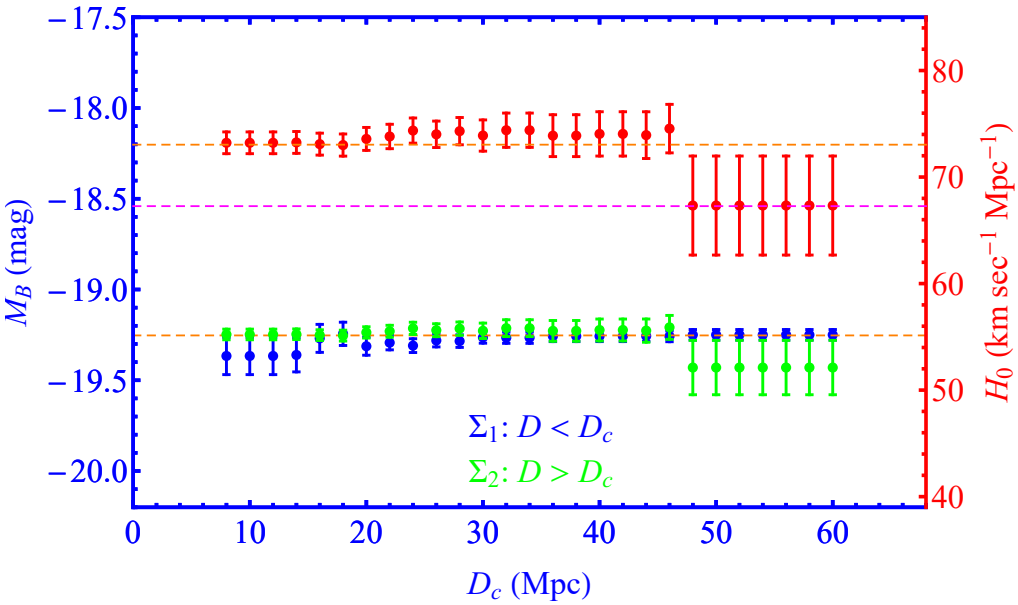

Figure 8. The best-fit values with uncertainties for the high–low D bin of SnIa absolute magnitude M_B (green and blue points) and for H_0 (red points). This generalization of the SH0ES baseline analysis allows for a transition of M_B. The best-fit parameter values as shown as functions of the critical transition D_c. Dotted lines correspond to the SH0ES R21 best fit and to the Planck18/ΛCDM best fit for H_0.

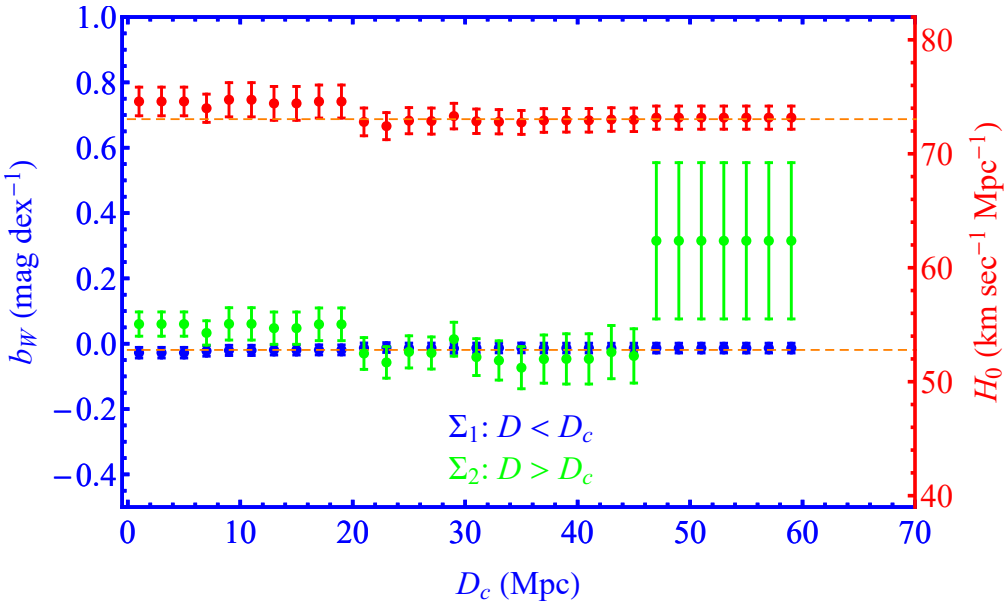

Figure 9. Same as Figure 8 in an analysis generalization, where the parameter b_W is allowed to have a transition at a distance D_c. Notice the sharp increase in the difference between best-fit parameters high of D and low D bin $|b_W^> - b_W^<|$ for $D_c > 47$ Mpc.

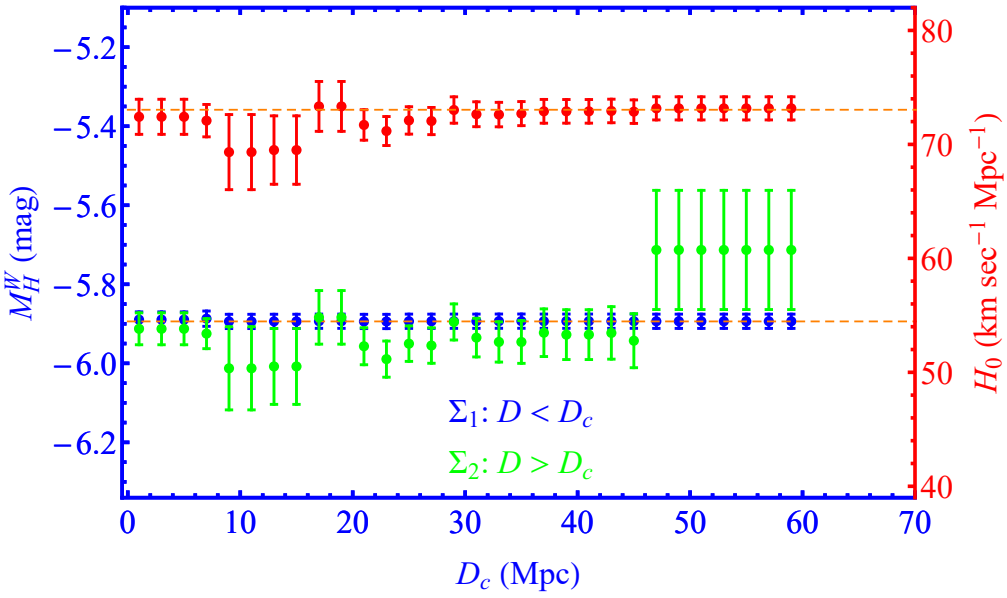

Figure 10. Same as Figure 8 in an analysis generalization, where the parameter M_W is allowed to have a transition at a distance D_c. Notice the sharp increase in the difference between best-fit parameters of high D and low D bin $|M_W^> - M_W^<|$ for $D_c > 47$ Mpc.

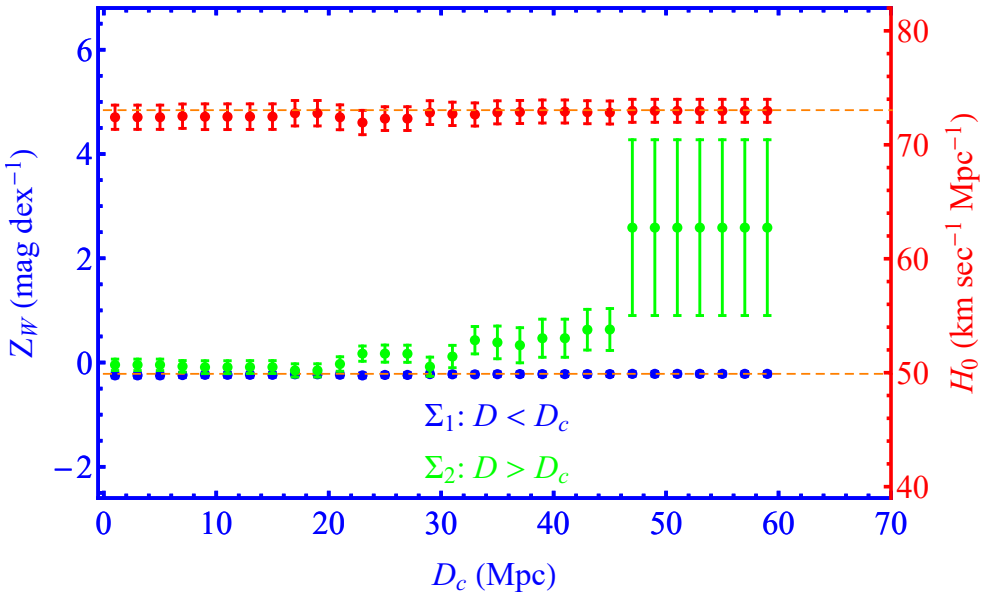

Figure 11. Same as Figure 8 in an analysis generalization where the parameter Z_W is allowed to have a transition at a distance D_c. Notice the sharp increase in the difference between best fit parameters of high D and low D bin $|Z_W^{>} - Z_W^{<}|$ for $D_c > 47$ Mpc. The best-fit value of the Hubble parameter (red points) is not significantly affected by this type of degree of freedom perhaps due to the indirect connection of Z_W with H_0.

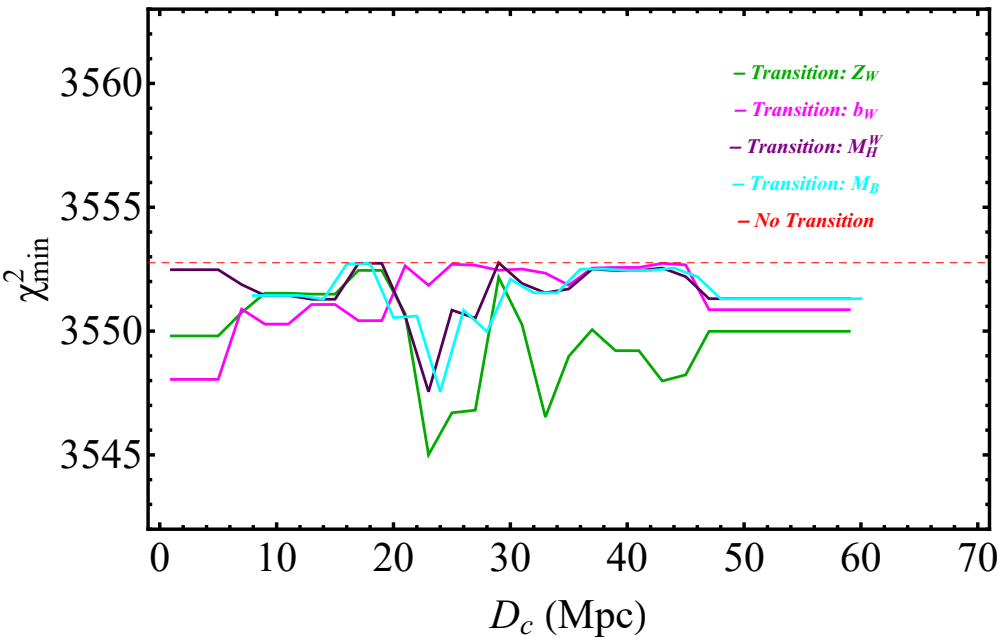

Figure 12. The values of $\Delta\chi^2_{min}$ in terms of D_c for the four transition models considered with respect to the SH0ES baseline model. No inverse distance ladder constraint on M_B is used for either the baseline or the transition models. The small improvement of the fit to the data is not enough to justify any model preference.

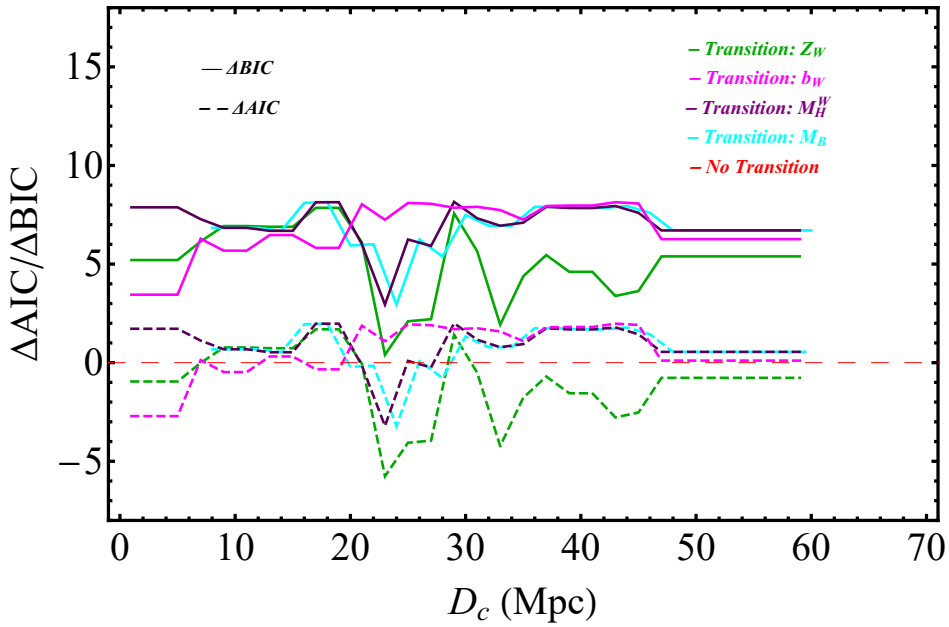

Figure 13. The values of ΔAIC and ΔBIC in terms of D_c for the four transition models considered with respect to the SH0ES baseline model. No inverse distance ladder constraint on M_B is used for either the baseline or the transition models. The small improvement of the χ^2 fit to the data is not enough to justify any model preference. In fact, the BIC which strongly penalizes any additional parameter mildly disfavors the transition models.

3.2. The Effect of the Inverse Distance Ladder Constraint

In view of the spontaneous transition of the SnIa absolute magnitude M_B that appears to lead to a Hubble tension resolution, while being mildly favored by the SH0ES data ($\Delta\chi^2 \simeq -1.5$) without any inverse distance ladder information included in the fit, the following question arises:

How does the level of preference for the M_B transition model (compared to the SH0ES baseline model) change if an additional constraint is included in the analysis obtained from the inverse distance ladder best fit for M_B?

The inverse distance ladder constraint on M_B is [149,160,161]

$$M_B^{P18} = -19.401 \pm 0.027 \tag{35}$$

In order to address this question, we modify the analysis by adding one more constraint to the **Y** data vector: after entry 3215, which corresponds to the 8th constraint, we add the value -19.401 for the M_B constraint. We also add a line to the model matrix **L** after line 3215 with all entries set to zero except the entry at column 43 corresponding to the parameter $M_B^<$. A column after column 43 is added in **L** to accommodate the high distance parameter $M_B^>$ as described above. The new constraint is assigned a large distance (larger than the distance of the most distant SnIa of the sample) so that it only affects the high-distance parameter $M_B^>$ (the entry at line 3216 column 43 of **L** is set to 0 for all D_c, while the entry at column 44 of the same line is set to 1 for all D_c). To accommodate the corresponding uncertainty of the new constraint, we also add a line at the covariance matrix after line 3215 with a single nonzero entry at the diagonal equal to $\sigma_{MB}^2 = 0.027^2 = 0.000729$. Thus, after the implementation of the constraint in the M_B transition model, the **Y** vector has 3493 entries, the **L** model matrix has dimensions 3493×48, the **q** parameter vector has 48 entries, and the covariance matrix **C** matrix has dimensions 3493×3493. In a similar way, we may implement the constraint (35) in the SH0ES model without allowing for the additional transition degree of freedom and implement model selection criteria to compare the baseline with the transition model in the presence of the inverse distance ladder constraint.

The new constraints on H_0 and on the parameters $M_B^<$, $M_B^>$ emerging from this modified modeling analysis are shown in Figure 14 in terms of D_c. The corresponding quality of fit expressed via the value of χ^2_{min} and model selection [162,163] expressed via the AIC [164] and BIC criteria is shown in Figure 15. The definitions and properties of the AIC and BIC criteria are described in Appendix D

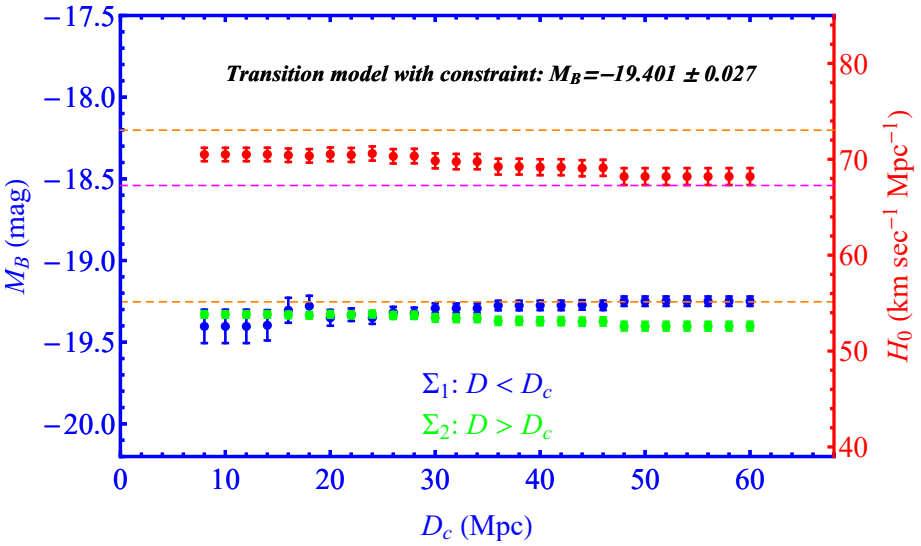

Figure 14. The new constraints on H_0 and on the parameters $M_B^<$, $M_B^>$ emerging after implementing the inverse distance ladder constraint (35) on the high-distance bin of the M_B transition model.

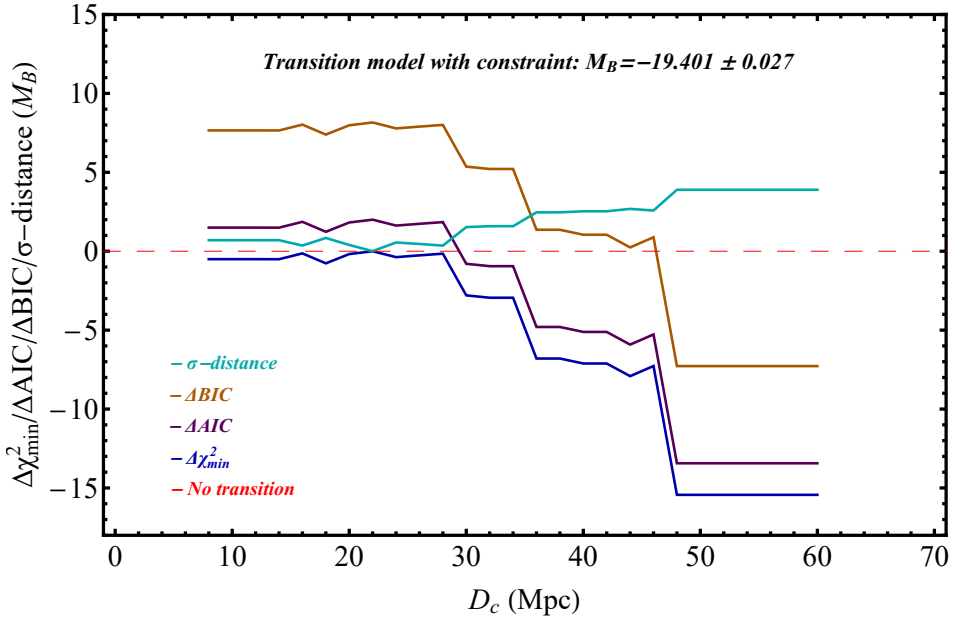

Figure 15. Model selection criteria of the M_B transition model with respect to the baseline SH0ES model in the presence of the inverse distance ladder constraint (35). The σ-distance between the low-distance best-fit $M_B^<$ and the high-distance $M_B^>$ is also plotted in terms of D_c. Clearly, the M_B transition model is strongly preferred with respect to the SH0ES baseline (no transition) model, especially for transition distances $D_c \simeq 50$ Mpc.

Clearly, the transition degree of freedom at $D_c \simeq 50$ Mpc which is mildly preferred by the data, even in the absence of the inverse distance ladder constraint, is strongly preferred by the data in the presence of the constraint while the σ-distance between the low-distance best-fit parameter $M_B^<$ and the high distance $M_B^>$ reaches a level close to 4σ.

These results are described in more detail in Table 4. The full list of the best-fit values of all the parameters of the vector **q** for the SH0ES baseline model with and without the inverse distance ladder constraint in the data vector **Y** is shown in Table 2 along with the corresponding uncertainties.

Table 4. A model comparison (baseline vs transitions) and best-fit parameter values in the absence (top five rows) and in the presence (last two rows) of the inverse distance ladder constraint. Notice that in the presence of the inverse distance ladder constraint and the transition degree of freedom, the best-fit value of H_0 is identical to the inverse distance ladder result of the completed SDSS-IV extended BAO survey [35].

Model	χ^2_{min}	χ^2_{red} [a]	ΔAIC	ΔBIC	H_0 km s^{-1} Mpc^{-1}	M_B [mag]	M_H^W [mag]	Δb_W [mag/dex]	Z_W [mag/dex]
Baseline	3552.76	1.031	0	0	73.043 ± 1.007	-19.253 ± 0.029	-5.894 ± 0.018	-0.013 ± 0.015	-0.217 ± 0.045
Transition [b] M_B	3551.31	1.031	0.55	6.71	67.326 ± 4.647	-19.250 ± 0.029 -19.430 ± 0.150 1.2σ	-5.894 ± 0.018	-0.013 ± 0.015	-0.217 ± 0.045
Transition [b] M_H^W	3551.31	1.031	0.55	6.71	73.162 ± 1.014	-19.250 ± 0.029	-5.894 ± 0.018 -5.713 ± 0.151 1.2σ	-0.013 ± 0.015	-0.217 ± 0.045
Transition [b] Z_W	3549.99	1.030	-0.77	5.39	72.981 ± 1.007	-19.255 ± 0.029	-5.894 ± 0.018	-0.014 ± 0.015	-0.217 ± 0.045 2.588 ± 1.686 1.7σ
Transition [b] b_W	3550.86	1.030	0.10	6.26	73.173 ± 1.013	-19.249 ± 0.029	-5.894 ± 0.018	-0.013 ± 0.015 0.315 ± 0.239 1.4σ	-0.217 ± 0.045
Baseline+Constraint [c]	3566.78	1.035	0	0	70.457 ± 0.696	-19.332 ± 0.020	-5.920 ± 0.017	-0.026 ± 0.015	-0.220 ± 0.045
Transition [b,c] M_B **+ Constraint**	3551.34	1.031	-13.44	-7.27	68.202 ± 0.879	-19.249 ± 0.029 -19.402 ± 0.027 3.9σ	-5.893 ± 0.018	-0.013 ± 0.015	-0.217 ± 0.045

NOTE: (a) $\chi^2_{red} = \chi^2_{min}/dof$, where $dof = N - M$ is typically the number of degrees of freedom (with N the number of datapoints used in the fit and M the number of free parameters) for each model. (b) At critical distance $D_c \simeq 50$ Mpc. (c) With constraint $M_B = -19.401 \pm 0.027$.

The following comments can be made on the results shown in Table 4.

- The M_B transition degree of freedom resolves the H_0 tension both in the absence of the inverse distance ladder constraint (second raw of Table 4) and in the presence of it (last row of Table 4).
- In the presence of the inverse distance ladder constraint, the model with the M_B transition degree of freedom at $D_c = 50$ Mpc is strongly preferred over the baseline *SH0ES* model as indicated by the model selection criteria, despite the additional parameter it involves (comparison of the last two rows of Table 4).
- The transition degree of freedom, when allowed in each of the other three modeling parameters, does not lead to a spontaneous resolution of the Hubble tension since the best-fit value of H_0 is not significantly affected. However, it does induce an increased absolute difference between the best-fit values of the high-distance and low-distance parameters, which, however, is not statistically significant due to the large uncertainties of the bin with $D > D_c \simeq 50$ Mpc (see also Figures 9–11).

The above comments indicate that interesting physical and or systematic effects may be taking place at distances at or beyond 50 Mpc in the SH0ES data, and therefore more and better quality Cepheid/SnIa data are needed at these distances to clarify the issue. This point is further enhanced by the recent study of Ref. [117], indicating that SnIa in the Hubble flow (at distances $D > 90$ Mpc) appear to have different color calibration properties than SnIa in Cepheid hosts (at distances $D < 75$ Mpc).

The hints for a transition in the SnIa absolute luminosity and magnitude M_B are also demonstrated in Figure 16, where we show the mean[14] SnIa absolute magnitude M_{Bi} for each Cepheid+SnIa host i is obtained from the equation

$$M_{Bi} = m^0_{Bi} - \mu_i \tag{36}$$

where m^0_{Bi} is the measured apparent magnitude of the SnIa, and μ_i are the best-fit distance host distance moduli obtained using the SH0ES baseline model (left panel of Figure 16) and the M_B transition model (right panel), which allows (but does not enforce) an M_B transition at $D_c = 50$ Mpc. Notice that when the M_B transition degree of freedom is allowed in the analysis, the best-fit values of M_{Bi} for the more distant hosts N0976 ($D = 60.5$ Mpc) and N0105 ($D = 73.8$ Mpc) spontaneously drop to the inverse distance ladder calibrated value range.

The inverse distance ladder calibrated values of the absolute magnitudes M_{Bi} of SnIa in the Hubble flow are obtained by assuming $H_0 = H_0^{P18} = 67.36 \pm 0.54$ km s^{-1} Mpc^{-1} and using the following equation

$$M_{Bi} = m(z^0_{Bi}) + 5\log_{10}\left[H_0^{P18} \cdot Mpc/c\right] - 5\log_{10}[D_L(z_i)] - 25 \tag{37}$$

where $D_L(z_i)$ is the Hubble free luminosity distance in the context of Planck18/ΛCDM and $m(z^0_{Bi})$ are the binned corrected SnIa apparent magnitudes of the Pantheon sample. The corresponding binned Cepheid+SnIa host values of M_B obtained assuming the baseline Sh0ES model (red points) and the M_B transition model ($D_c = 50$ Mpc, green points) are shown in Figure 17 along with the inverse distance ladder calibrated binned M_B of the Hubble flow SnIa of the Pantheon dataset (blue points). When the transition dof is allowed, the data excite it, and a hint for a transition appears (the green data point of the transition model is clearly below the red point corresponding to the constant M_B SH0ES baseline model), even though the statistical significance of the indicated transition is low due to the small number of Cepheids (41) included in the last bin with $D \in [50$ Mpc,75 Mpc].

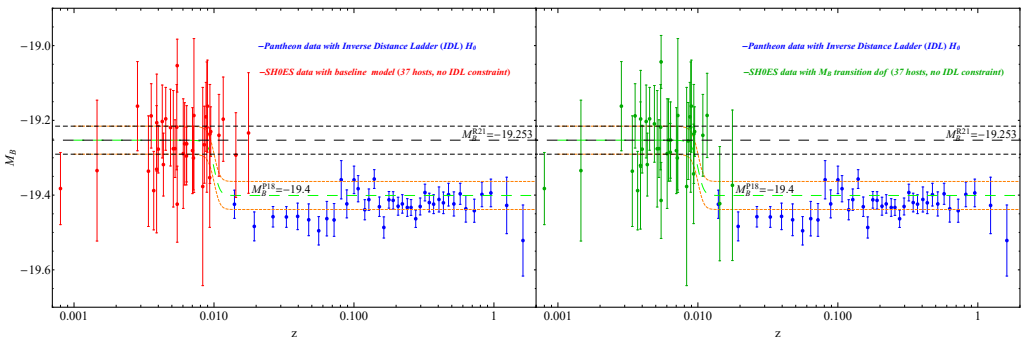

Figure 16. The mean SnIa absolute magnitude M_{Bi} for each Cepheid+SnIa host i obtained from Equation (36), obtained using the SH0ES baseline model (left panel) and the M_B transition model (right panel), which allows (but does not enforce) an M_B transition at $D_c = 50$ Mpc. Notice that when the M_B transition degree of freedom is allowed in the analysis, the best-fit values of M_{Bi} for the more distant hosts N0976 ($D = 60.5$ Mpc) and N0105 ($D = 73.8$ Mpc) spontaneously drop to the inverse distance ladder calibrated value range (green points with $z > 0.01$).

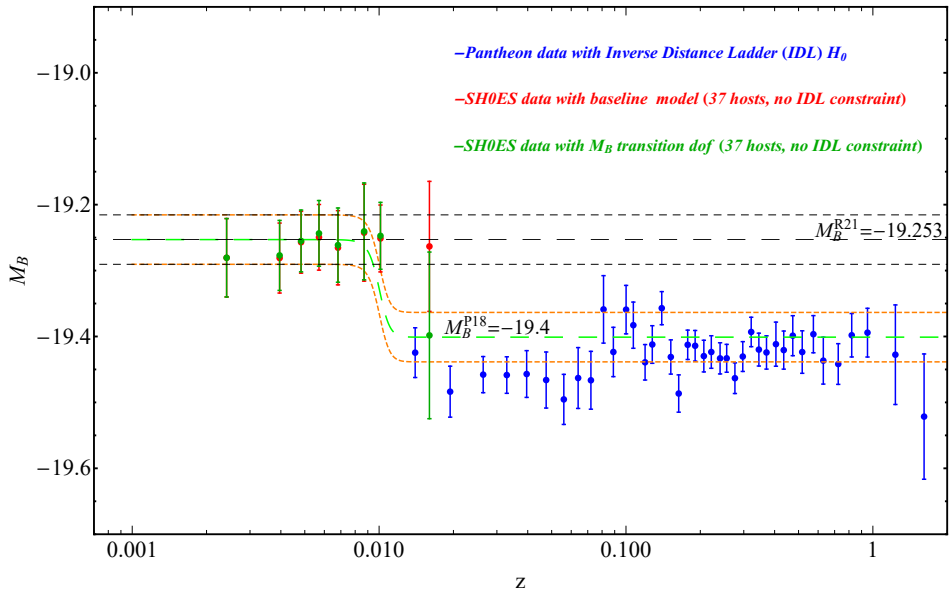

Figure 17. The binned (5 host bins with 2 hosts in last bin where $z > 0.01$) Cepheid+SnIa host values of M_B obtained assuming the baseline SH0ES model (red points) and the M_B transition model ($D_c = 50$ Mpc, green points) are shown along with the inverse distance ladder calibrated binned M_B of the Hubble flow SnIa of the Pantheon dataset (blue points). When the transition dof is allowed, the data excite it, and a hint of a transition appears (the green data point of the transition model is clearly below the red point corresponding to the constant M_B SH0ES baseline model).

4. Conclusions

We described a general framework for the generalization of the Cepheid+SnIa modeling in the new SH0ES data. Such a modeling generalization approach is motivated by the increased statistical significance of the Hubble tension and may hint toward new degrees of freedom favored by the data. Such degrees of freedom may be attributed to either new physics or to unknown systematics hidden in the data.

In the present analysis, we focused on a particular type of new modeling degree of freedom, allowing for the transition of any one of the four Cepheid/SnIa modeling parameters at a distance D_c. However, our analysis can be easily extended to different degrees of freedom with physical motivation. Examples include possible modeling parameter dependence on properties other than distance (e.g., dust extinction and color and stretch calibration properties). In addition, other degrees of freedom that could be excited by the data could involve the modeling parameters that have been absorbed in the R21 SH0ES data, such as the Cepheid dust extinction parameter R_W and the color and stretch SnIa calibration parameters β and α. These degrees of freedom may also be probed and excited by the fit to the data if allowed by the modeling [117].

We demonstrated that our proposed transition degrees of freedom are mildly excited by the SH0ES data, and in the case of the SnIa absolute magnitude M_B transition degree of freedom at $D_c \simeq 50$ Mpc, the best-fit value of H_0 shifts spontaneously to a value almost identical to the Planck18/ΛCDM best-fit value, thus annihilating the Hubble tension. However, the high-distance bin in this case involves only 41 Cepheids and 4 SnIa, and therefore, the best-fit value of $M_B^>$, which effectively also fixes H_0, involves significant uncertainties.

In the presence of the inverse distance ladder constraint on the high-distance bin parameter $M_B^>$ of the M_B transition model and on the single M_B parameter of the SH0ES model, the uncertainties reduce dramatically. The Hubble tension is fully resolved only in the presence of the M_B transition degree of freedom at $D_c \simeq 50$ Mpc. This transition model is also strongly selected over the baseline SH0ES model with the constraint, by both model selection criteria AIC and BIC, despite the penalty imposed by AIC and especially BIC on the additional parameter involved in the new modeling. This behavior along with other

recent studies [117] hints toward the need of more detailed Cepheid+SnIa calibrating data at distances $D \gtrsim 50$ Mpc, i.e., at the high end of rung two on the distance ladder.

Our comprehensively described generalized modeling approach opens a new direction in the understanding of the Hubble tension and may be extended by the introduction of a wide range of new degrees of freedom in the SH0ES data analysis and also by the introduction of new constraints motivated by other cosmological data. Such extensions could, for example, involve more distance bins in the distance dependence of the four main modeling parameters. In that case, the relevant column of the modeling matrix **L** would have to be replaced by more than two columns (one for each distance bin). Such bins could also be defined not in terms of distance, but in terms of other Cepheid/SnIa properties (e.g., Cepheid metallicity or period and/or SnIa light curve color or stretch). In addition, other parameters beyond the four basic modeling parameters may be considered, including the dust extinction parameter R_W and/or the SnIa light curve color and stretch parameters. Additionally, similar modeling generalizations may be implemented on different distance calibrator data used for the measurement of H_0, such as the TRGB data [165].

Physical motivation is an important factor for the evaluation of any new modeling degree of freedom, especially if it is favored by the data. A transition of the SnIa luminosity at a particular recent cosmic time could be induced by a sudden change of the value of a fundamental physics constant, e.g., the gravitational constant in the context of a recent first-order phase transition [166–168] to a new vacuum of a scalar–tensor theory, or in the context of a generalization of the symmetron screening mechanism [143]. A similar first-order transition was implemented in early dark energy models [169], attempting to change the last scattering sound horizon scale without affecting other well-constrained cosmological observables. Thus, even though no relevant detailed analysis has been performed so far, there are physical mechanisms that could potentially induce the SnIa luminosity transition degree of freedom.

The emerging new puzzles challenging our standard models may soon pave the way to exciting discoveries of new physical laws. The path to these discoveries goes through the deep and objective understanding of the true information that is hidden in the cosmological data. The present analysis may be a step in that direction.

Author Contributions: Conceptualization: L.P.; methodology: L.P. and F.S.; software: L.P. and F.S.; data curation: F.S.; investigation: F.S. All authors have read and agreed to the published version of the manuscript.

Funding: This work was supported by the Hellenic Foundation for Research and Innovation (HFRI-Progect No: 789).

Data Availability Statement: The numerical analysis files for the reproduction of the figures can be found in the A reanalysis of the SH0ES data for H_0 GitHub repository, https://github.com/FOTEINISKARA/A-reanalysis-of-the-SH0ES-data-for-H_0, (accessed on 23 August 2022) under the MIT license.

Acknowledgments: We thank Adam Riess, Dan Scolnic, Eoin Colgain, and Radoslaw Wojtak for useful comments.

Conflicts of Interest: The authors declare no conflict of interest.

Appendix A. Covariance Matrix

A schematic form of the non-diagonal covariance matrix used in our analysis is shown below. The symbols $\sigma^2_{tot,i}$ indicate the (non-diagonal in general) covariance submatrix within the i host, while the symbols Z_{cov} indicate submatrices that correlate the uncertainties between different hosts.

$$
\mathbf{C} = \left(\begin{array}{cccccccccccccccccccccccccc}
\sigma^2_{tot,1} & \dots & Z_{cov} & & & & & & & & & & & & & & & & & & & & & & & \\
\dots & \dots & \dots & Z_{cov} & & & & & & & & & & & & & & & & & & & & & \\
Z_{cov} & \dots & \sigma^2_{tot,37} & & Z_{cov} & & & & & & & & & & & & & & & & & & & & \\
\hline
Z_{cov} & \dots & Z_{cov} & \sigma^2_{tot,N4258} & 0 & 0 & 0 & 0 & \dots & 0 & 0 & 0 & \dots & 0 & 0 & 0 & \dots & 0 & 0 & 0 & \dots & 0 & 0 & 0 & \dots & 0 \\
0 & \dots & 0 & 0 & \sigma^2_{tot,M31} & 0 & 0 & 0 & \dots & 0 & 0 & 0 & \dots & 0 & 0 & 0 & \dots & 0 & 0 & 0 & \dots & 0 & 0 & 0 & \dots & 0 \\
0 & \dots & 0 & 0 & 0 & \sigma^2_{tot,LMC} & 0 & 0 & \dots & 0 & 0 & 0 & \dots & 0 & 0 & 0 & \dots & 0 & 0 & 0 & \dots & 0 & 0 & 0 & \dots & 0 \\
\hline
0 & \dots & 0 & 0 & 0 & 0 & \sigma^2_{M_B,1} & \dots & Sn_{cov} & 0 & 0 & 0 & \dots & 0 & 0 & 0 & \dots & 0 & 0 & 0 & \dots & 0 & Sn_{cov} & \dots & Sn_{cov} & \\
\dots & \dots & \dots & \dots & \dots & \dots & \dots & \dots & \dots & \dots & \dots & \dots & \dots & \dots & \dots & \dots & \dots & \dots & \dots & \dots & \dots & \dots & \dots & \dots & \dots & \\
0 & \dots & 0 & 0 & 0 & 0 & Sn_{cov} & \dots & \sigma^2_{M_B,77} & 0 & 0 & 0 & \dots & 0 & 0 & 0 & \dots & 0 & 0 & 0 & \dots & 0 & Sn_{cov} & \dots & Sn_{cov} & \\
\hline
0 & \dots & 0 & 0 & 0 & 0 & 0 & \dots & 0 & \sigma^2_{M^W_H,HST} & 0 & 0 & \dots & 0 & 0 & 0 & \dots & 0 & 0 & 0 & \dots & 0 & 0 & 0 & \dots & 0 \\
0 & \dots & 0 & 0 & 0 & 0 & 0 & \dots & 0 & 0 & \sigma^2_{M^W_H,Gaia} & 0 & \dots & 0 & 0 & 0 & \dots & 0 & 0 & 0 & \dots & 0 & 0 & 0 & \dots & 0 \\
0 & \dots & 0 & 0 & 0 & 0 & 0 & \dots & 0 & 0 & 0 & \sigma^2_{Z_W,Gaia} & \dots & 0 & 0 & 0 & \dots & 0 & 0 & 0 & \dots & 0 & 0 & 0 & \dots & 0 \\
0 & \dots & 0 & 0 & 0 & 0 & 0 & \dots & 0 & 0 & 0 & 0 & \dots & \sigma^2_x & 0 & 0 & \dots & 0 & 0 & 0 & \dots & 0 & 0 & 0 & \dots & 0 \\
0 & \dots & 0 & 0 & 0 & 0 & 0 & \dots & 0 & 0 & 0 & 0 & \dots & 0 & \sigma^2_{ground,zp} & 0 & \dots & 0 & 0 & 0 & \dots & 0 & 0 & 0 & \dots & 0 \\
0 & \dots & 0 & 0 & 0 & 0 & 0 & \dots & 0 & 0 & 0 & 0 & \dots & 0 & 0 & \sigma^2_{b_W} & \dots & 0 & 0 & 0 & \dots & 0 & 0 & 0 & \dots & 0 \\
0 & \dots & 0 & 0 & 0 & 0 & 0 & \dots & 0 & 0 & 0 & 0 & \dots & 0 & 0 & 0 & \dots & \sigma^2_{\mu,N4258} & 0 & 0 & \dots & 0 & 0 & 0 & \dots & 0 \\
0 & \dots & 0 & 0 & 0 & 0 & 0 & \dots & 0 & 0 & 0 & 0 & \dots & 0 & 0 & 0 & \dots & 0 & \sigma^2_{\mu,LMC} & 0 & \dots & 0 & 0 & 0 & \dots & 0 \\
\hline
0 & \dots & 0 & 0 & 0 & 0 & Sn_{cov} & \dots & Sn_{cov} & 0 & 0 & 0 & \dots & 0 & 0 & 0 & \dots & 0 & 0 & \sigma^2_{M_B,z,1} & \dots & Sn_{cov} & & & & \\
\dots & \dots & \dots & \dots & \dots & \dots & \dots & \dots & \dots & \dots & \dots & \dots & \dots & \dots & \dots & \dots & \dots & \dots & \dots & \dots & \dots & \dots & & & & \\
0 & \dots & 0 & 0 & 0 & 0 & Sn_{cov} & \dots & Sn_{cov} & 0 & 0 & 0 & \dots & 0 & 0 & 0 & \dots & 0 & 0 & Sn_{cov} & \dots & \sigma^2_{M_B,z,277} & & & &
\end{array}\right)
$$

Appendix B. Analytic Minimization of χ^2

The proof of Equations (19) and (20) that lead to the best-fit parameter values and their uncertainties through the analytic minimization of χ^2 may be sketched as follows[15]:

Using the matrix of measurements (data vector) **Y**, the matrix of parameters **q** and the equation (or design) matrix **L** with the measurement error matrix (covariance matrix) **C**, the χ^2 statistic is expressed as

$$\chi^2 = (\mathbf{Y} - \mathbf{Lq})^{\mathbf{T}}\mathbf{C}^{-\mathbf{1}}(\mathbf{Y} - \mathbf{Lq}) = \mathbf{q}^{\mathbf{T}}\mathbf{L}^{\mathbf{T}}\mathbf{C}^{-\mathbf{1}}\mathbf{Lq} - \mathbf{2q}^{\mathbf{T}}\mathbf{L}^{\mathbf{T}}\mathbf{C}^{-\mathbf{1}}\mathbf{Y} + \mathbf{Y}^{\mathbf{T}}\mathbf{C}^{-\mathbf{1}}\mathbf{Y} \quad \text{(A1)}$$

The χ^2 is minimized with respect to the parameters $\mathbf{q}$ by solving the equation

$$\frac{\partial \chi^2}{\partial \mathbf{q}}\Big|_{\mathbf{q}_{best}} = 0 => \mathbf{2L}^{\mathbf{T}}\mathbf{C}^{-\mathbf{1}}\mathbf{Lq}_{\mathbf{best}} - \mathbf{2L}^{\mathbf{T}}\mathbf{C}^{-\mathbf{1}}\mathbf{Y} = \mathbf{0} \quad \text{(A2)}$$

Thus, the maximum-likelihood parameters are given as

$$\mathbf{q}_{best} = (\mathbf{L}^{\mathbf{T}}\mathbf{C}^{-\mathbf{1}}\mathbf{L})^{-\mathbf{1}}\mathbf{L}^{\mathbf{T}}\mathbf{C}^{-\mathbf{1}}\mathbf{Y} \quad \text{(A3)}$$

We tested the validity of this equation numerically by calculating χ^2 for the SH0ES baseline model and showing that, indeed, it has a minimum at the analytically predicted parameter values provided by (A3). This is demonstrated in Figure A1, where we show $\chi^2(H_0)$ with the rest of the parameters fixed at their analytically predicted best-fit values. As expected, the minimum is obtained at the analytically predicted value of H_0.

The standard errors squared of the parameters in $\mathbf{q}_{\mathbf{best}}$ are given as the diagonal elements of the transformed covariance matrix

$$\Sigma_{\mathbf{kl}} = \sum_{\mathbf{i}}\sum_{\mathbf{j}}\left[\frac{\partial \mathbf{q}_{\mathbf{best,k}}}{\partial \mathbf{Y_i}}\right]\mathbf{C_{ij}}\left[\frac{\partial \mathbf{q}_{\mathbf{best,l}}}{\partial \mathbf{Y_j}}\right] \quad \text{(A4)}$$

or

$$\Sigma = \left[\frac{\partial \mathbf{q}_{\mathbf{best}}}{\partial \mathbf{Y}}\right]\mathbf{C}\left[\frac{\partial \mathbf{q}_{\mathbf{best}}}{\partial \mathbf{Y}}\right]^{\mathbf{T}} \quad \text{(A5)}$$

Thus,

$$\Sigma = (\mathbf{L}^{\mathbf{T}}\mathbf{C}^{-\mathbf{1}}\mathbf{L})^{-\mathbf{1}}\mathbf{L}^{\mathbf{T}}\mathbf{C}^{-\mathbf{1}}\mathbf{C}\left[(\mathbf{L}^{\mathbf{T}}\mathbf{C}^{-\mathbf{1}}\mathbf{L})^{-\mathbf{1}}\mathbf{L}^{\mathbf{T}}\mathbf{C}^{-\mathbf{1}}\right]^{\mathbf{T}} \quad \text{(A6)}$$

$$= (\mathbf{L}^{\mathbf{T}}\mathbf{C}^{-\mathbf{1}}\mathbf{L})^{-\mathbf{1}}\mathbf{L}^{\mathbf{T}}\mathbf{C}^{-\mathbf{1}}\mathbf{C}\mathbf{C}^{-\mathbf{1}}\mathbf{L}(\mathbf{L}^{\mathbf{T}}\mathbf{C}^{-\mathbf{1}}\mathbf{L})^{-\mathbf{1}} \quad \text{(A7)}$$

$$= (\mathbf{L}^{\mathbf{T}}\mathbf{C}^{-\mathbf{1}}\mathbf{L})^{-\mathbf{1}} \quad \text{(A8)}$$

The standard errors provided by the equation for the SH0ES baseline model are consistent and almost identical to the published results of R21.

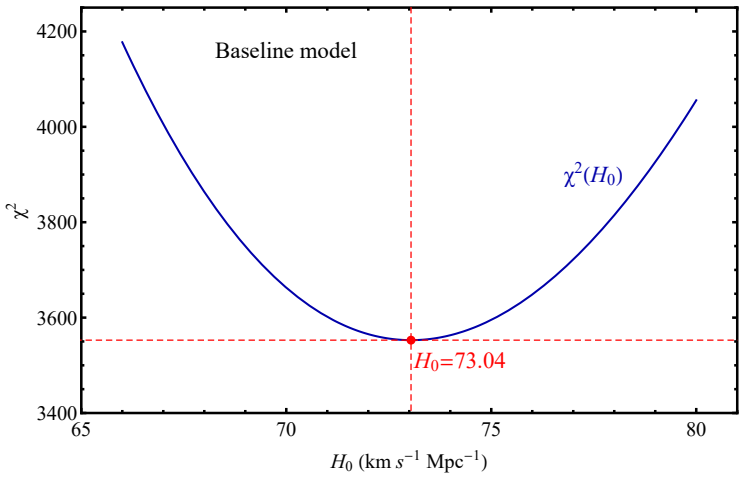

Figure A1. The form of $\chi^2(H_0)$ for the SH0ES baseline model has a minimum at the analytically predicted value of H_0 provided by (A3) (the rest of the parameters are fixed at their analytically predicted best-fit values).

Appendix C. Reanalysis of Individual Cepheid m_H^W Slope Data

We use the released Cepheid P-L data ($m_H^W - \log P$) to find the best-fit slope b_W in each one of the 40 Cepheid hosts, where the 3130 Cepheid magnitudes are distributed. We thus reproduce Figures 9 and 10 of R21. Since the released Cepheid magnitude data do not include outliers, we focus on the reproduction of the black points of Figure 10 of R21. Our motivation for this attempt includes the following:

- It is evident by inspection of Figure 10 of R21 (see also Figure A4 below) that most of the better measured b_W slopes have a smaller absolute slope than the corresponding slopes obtained from anchors+MW hosts. This makes it interesting to further test the homogeneity of these measurements and their consistency with the assumption of a global value of b_W for both anchors and SnIa hosts.
- Most of the measurements that include outliers (red points of Figure 10 of R21) tend to amplify the above-mentioned effect, i.e., they have smaller absolute slopes b_W than the slopes obtained from the anchors.
- The slope corresponding to the host N4424 is missing from Figure 10 of R21, while the host M1337 appears to show extreme behavior of the outliers.

Based on the above motivation, we recalculated all the b_W slopes of the Cepheid hosts and also extended the analysis to metallicity slopes for the Cepheids of each hosts. The individual metallicity slopes $Z_{W,i}$ for each host were obtained for the first time in our analysis and thus, no direct comparison can be made with R21 for these slopes.

The Cepheid magnitude period and magnitude metallicity data used to calculate the corresponding best-fit slopes b_W and Z_W are shown in Figures A2 and A3 for each host along with the best-fit straight lines from which the individual best-fit $b_{W,i}$ and $Z_{W,i}$ were obtained. The numerical values of the derived best-fit slopes along with the corresponding uncertainties are shown in Table A1.

The derived best-fit slopes $b_{W,i}$ for each host along with their standard errors (obtained using Equations (25) and (26)) are shown in Figure A4 (purple points) along with the corresponding points of Figure 10 of R21 (green points).

The best-fit values of the slopes $b_{W,i}$ we obtained using the raw Cepheid data are consistent with Figure 10 of R21 as shown in Figure A4. The agreement with the results of R21 is excellent, except for three points. Two slopes corresponding to the hosts N4038 and N1365 are slightly shifted in our analysis compared to R21, due a small disagreement in the best-fit slope and a typo of R21 in transferring the correct slope to Figure 10.

In addition, the slope corresponding to the host N4424 is missing in Figure 10 of R21. In the $m_H^W - \log P$ plot of R21 (their Figure 9, where the magnitudes decrease upward on the vertical axis) corresponding to N4424, the indicated best fit line is the green line shown in the upper right inset plot of Figure A4 corresponding to the green point. The correct best fit, however, corresponds to the purple line of the upper right inset plot with the slope given by the purple point pointed by the arrow.

Thus, our Figure A4 is in excellent agreement with Figure 10 of R21 with the exception of three points, where our plot corrects the corresponding plot of R21. In any case, we stress that these three points do not play a significant role in our conclusion about the inhomogeneities of b_W and Z_W discussed in Section 2.2.

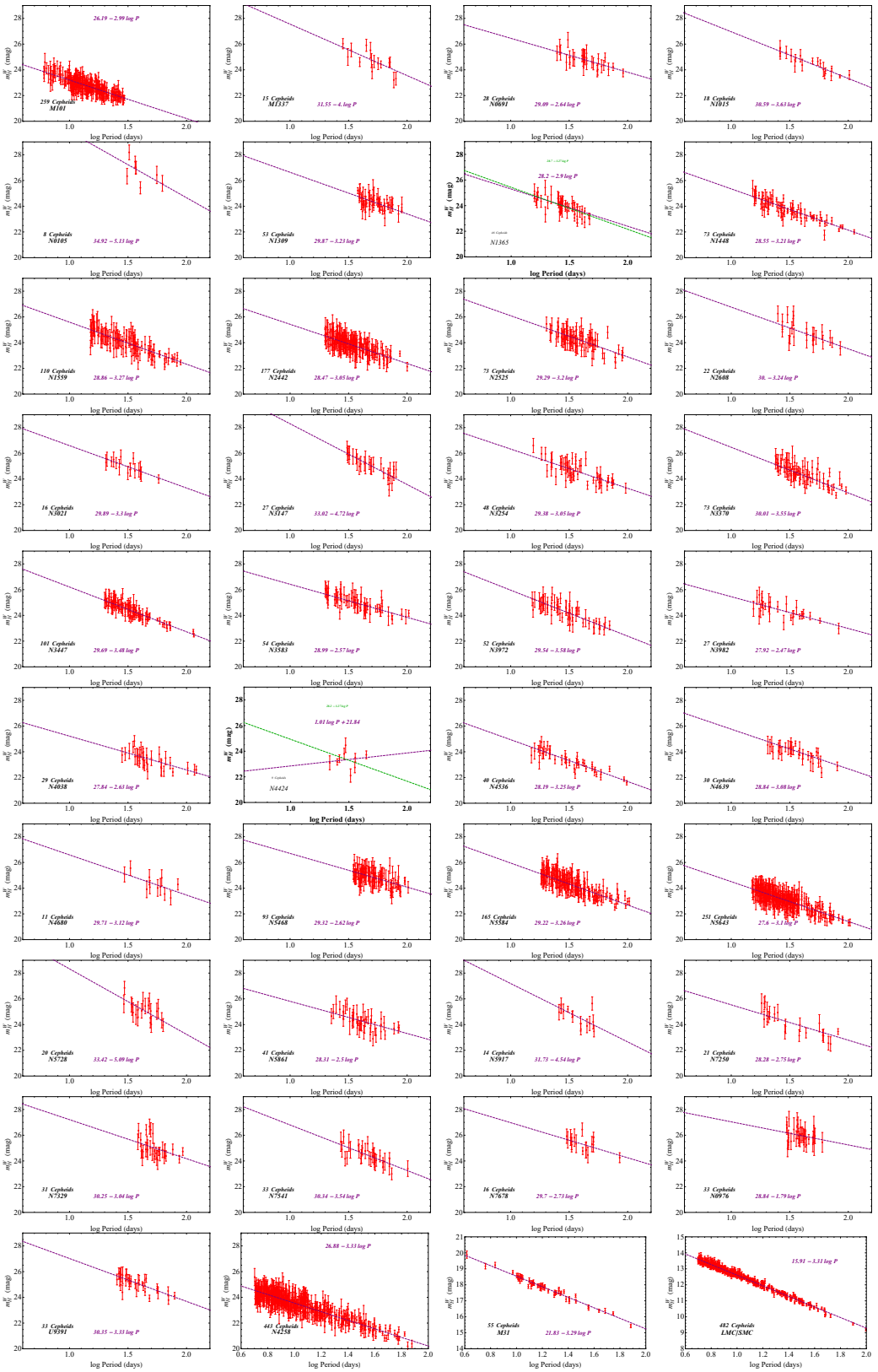

Figure A2. Fitting individual slopes b_W of the $m_H^W - \log P$, P-L relations for 40 Cepheid hosts: 37 SnIa+Cepheid hosts, 2 anchors (N4258+LMC/SMC) and the pure Cepheid host M31. In the case of the SnIa+Cepheid host N4424, our fit (purple line) is not in agreement with the fit of R21 (green line). In all other cases, the agreement is very good.

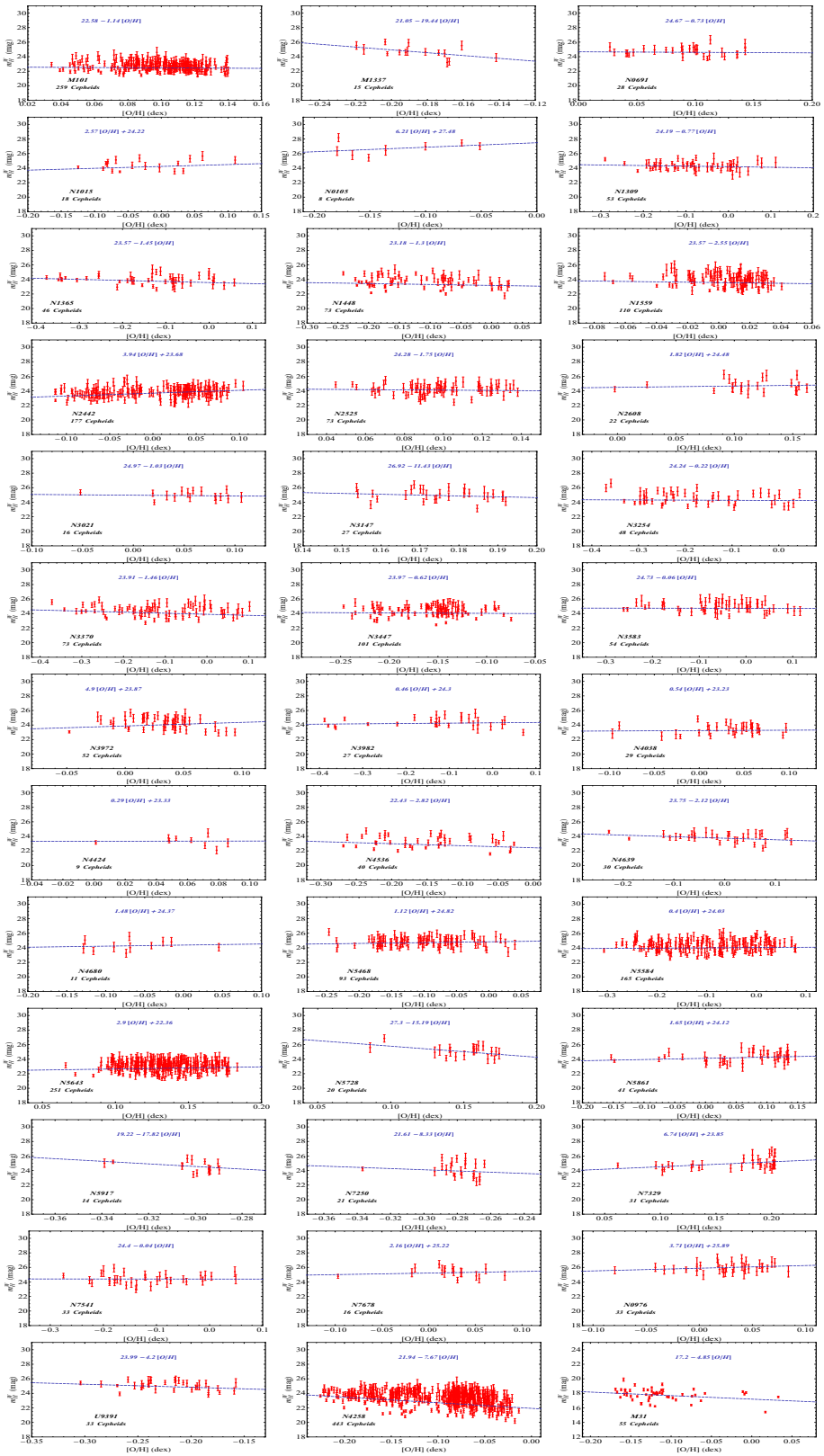

Figure A3. Fitting individual slopes Z_W of the m_H^W metallicity relations to Cepheid data for the hosts where individual Cepheid metallicity data were provided by R21 (only an average metallicity was provided for LMC/SMC and thus these Cepheid hosts are not included in the plot). Thus, the 39 hosts shown correspond to the 37 SnIa+Cepheid hosts, the anchor N4258 and the pure Cepheid host M31.

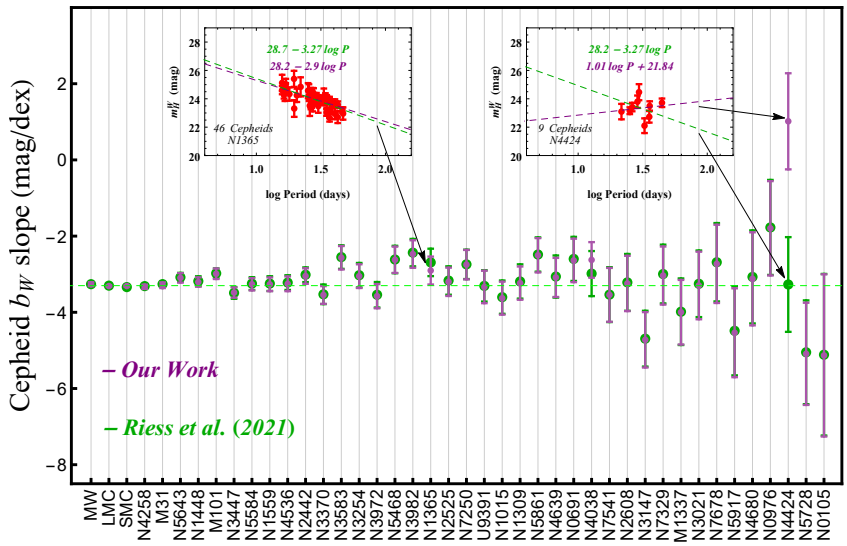

Figure A4. Independently-fitted slopes b_W of the m_H^W P-L relations (without background covariance of any pair of Cepheids as was done in R21, i.e., taking into account only diagonal terms of the covariance matrix). The points in green are the corresponding points shown in Figure 10 of R21 (obtained using plot digitizer). Our fits are in excellent agreement with R21, with the exception of 3 points corresponding to hosts N4424, N4038 and N1365. For N4424, there is no point shown in Figure 10 of R21 but in the corresponding $m_H^W - \log P$ plot of R21 (their Figure 9, where the magnitudes decrease upward on the vertical axis), the indicated best-fit line is the green line shown in the upper right inset plot corresponding to the green point. The correct best-fit, however, corresponds to the purple line of the upper right inset plot with slope given by the purple point pointed by the arrow. Similarly, the best-fit line corresponding to N1365 shown in the upper left inset plot is identical to our purple point and not to the green point. For the Milky Way (MW), we used directly the values provided in R21 obtained from Gaia EDR3+HST.

Table A1. The best-fit individual slopes b_W and Z_W with their standard errors σ and scatter uncertainties σ_{scat}. The scatter uncertainty ensures that the model of a universal best-fit slope becomes an acceptable model with $\chi^2_{min}/dof \simeq 1$, as described in Section 2.2. The number of hosts in the Table is $N = 42$, including the Milky Way (MW). For LMC and SMC, the metallicities are not provided individually for each Cepheid in R21, and thus no Z_W slope could be estimated in our analysis.

Galaxy	D [a] [Mpc]	b_W [mag/dex]	σ [mag/dex]	σ_{scat} [mag/dex]	Z_W [mag/dex]	σ [mag/dex]	σ_{scat} [mag/dex]
M101	6.71	−2.99	0.14	0.18	−1.14	0.86	3.2
M1337	38.53	−4.	0.85	0.18	−19.44	6.27	3.2
N0691	35.4	−2.64	0.57	0.18	−0.73	2.54	3.2
N1015	35.6	−3.63	0.43	0.18	2.57	1.3	3.2
N0105	73.8	−5.13	2.13	0.18	6.21	3.8	3.2
N1309	29.4	−3.23	0.44	0.18	−0.77	0.59	3.2
N1365	22.8	−2.9	0.37	0.18	−1.45	0.39	3.2
N1448	16.3	−3.21	0.12	0.18	−1.3	0.39	3.2
N1559	19.3	−3.27	0.18	0.18	−2.55	1.62	3.2
N2442	20.1	−3.05	0.2	0.18	3.94	0.58	3.2
N2525	27.2	−3.2	0.37	0.18	−1.75	2.74	3.2
N2608	35.4	−3.24	0.73	0.18	1.82	2.33	3.2
N3021	26.6	−3.3	0.89	0.18	−1.03	2.85	3.2
N3147	42.5	−4.72	0.73	0.18	−11.43	9.13	3.2
N3254	24.4	−3.05	0.31	0.18	−0.22	0.57	3.2
N3370	24	−3.55	0.23	0.18	−1.46	0.4	3.2
N3447	20.8	−3.48	0.13	0.18	−0.62	0.66	3.2
N3583	34.4	−2.57	0.31	0.18	−0.06	0.62	3.2
N3972	15.1	−3.58	0.32	0.18	4.9	1.58	3.2

Table A1. *Cont.*

Galaxy	D [a] [Mpc]	b_W [mag/dex]	σ [mag/dex]	σ_{scat} [mag/dex]	Z_W [mag/dex]	σ [mag/dex]	σ_{scat} [mag/dex]
N3982	19	−2.47	0.36	0.18	0.46	0.47	3.2
N4038	29.3	−2.63	0.47	0.18	0.54	2.07	3.2
N4424	16.4	1.01	1.26	0.18	0.29	4.33	3.2
N4536	31.9	−3.25	0.19	0.18	−2.82	0.56	3.2
N4639	19.8	−3.08	0.51	0.18	−2.12	0.64	3.2
N4680	42.1	−3.12	1.22	0.18	1.48	3.27	3.2
N5468	46.3	−2.62	0.35	0.18	1.12	0.74	3.2
N5584	28	−3.26	0.16	0.18	0.4	0.36	3.2
N5643	20.7	−3.1	0.12	0.18	2.9	1.17	3.2
N5728	44.9	−5.09	1.34	0.18	−15.19	5.71	3.2
N5861	30.3	−2.5	0.45	0.18	1.65	0.72	3.2
N5917	31	−4.54	1.17	0.18	−17.82	6.56	3.2
N7250	12.8	−2.75	0.39	0.18	−8.33	4.44	3.2
N7329	46.8	−3.04	0.76	0.18	6.74	1.86	3.2
N7541	34.4	−3.54	0.71	0.18	−0.04	1.08	3.2
N7678	46.6	−2.73	1.03	0.18	2.16	2.27	3.2
N0976	60.5	−1.79	1.24	0.18	3.71	2.73	3.2
U9391	29.4	−3.33	0.43	0.18	−4.2	1.51	3.2
N4258	7.4	−3.32	0.06	0.18	−7.67	0.31	3.2
M31	0.86	−3.29	0.07	0.18	−4.85	0.35	3.2
LMC [b]	0.05	−3.31	0.017	0.18	–	–	3.2
SMC [b]	0.06	−3.31	0.017	0.18	–	–	3.2
MW [c]	0	−3.26	0.05	0.18	−0.2	0.12	3.2

Note: (a) Distances from https://ned.ipac.caltech.edu/, (accessed on 23 August 2022). (b) No individual Cepheid metallicities were provided for LMC and SMC in R21 and thus we could not estimate the slope Z_W for these hosts. (c) For the Milky Way (MW), we directly used the values provided in R21 obtained from Gaia EDR3+HST.

Appendix D. Model Selection Criteria

Various methods for model selection have been developed and model comparison techniques have been used [162,163,170,171]. The reduced χ^2 is a very popular method for model comparison. This is defined by

$$\chi^2_{red} = \frac{\chi^2_{min}}{dof} \tag{A9}$$

where χ^2_{min} is the minimum χ^2, and $dof = N - M$ is typically the number of degrees of freedom (N is the number of datapoints used in the fit and M is the number of free parameters) for each model.

The model selection methods, such as the Akaike information criterion (AIC) [164] and the Bayesian information criterion (BIC) [172] that penalize models with additional parameters are used. For a model with M parameters and a dataset with N total observations, these are defined through the relations [163,170,171]

$$AIC = -2ln\mathcal{L}_{max} + 2M = \chi^2_{min} + 2M \tag{A10}$$

$$BIC = -2ln\mathcal{L}_{max} + MlnN = \chi^2_{min} + MlnN \tag{A11}$$

where $\mathcal{L}_{max} \equiv e^{-\chi^2_{min}/2}$ (e.g., [173,174]) is the maximum likelihood of the model under consideration.

The "preferred model" is the one which minimizes AIC and BIC. The absolute values of the AIC and BIC are not informative. Only the relative values between different competing models are relevant. Hence when comparing one model versus the baseline SH0ES, we can use the model differences ΔAIC and ΔBIC.

The differences ΔAIC and ΔBIC with respect to the baseline SH0ES model are defined as

$$\Delta AIC = AIC_i - AIC_s = \Delta\chi^2_{min} + 2\Delta M \tag{A12}$$

Table A2. The interpretation of differences ΔAIC and ΔBIC according to the calibrated Jeffreys' scale [175] (see also Refs. [170,174,176–178]). However, it should be noted that the Jeffreys' scale has to be interpreted with care [174] because it has been shown to lead to diverse qualitative conclusions.

ΔAIC			ΔBIC			
Level of empirical support for the model with the smaller AIC			Evidence against the model with the larger BIC			
0–2	4–7	>10	0–2	2–6	6–10	>10
Substantial	Strong	Very strong	Weak	Positive	Strong	Very strong

$$\Delta BIC = BIC_i - BIC_s = \Delta\chi^2_{min} + \Delta M(lnN) \tag{A13}$$

where the subindex i refers to value of AIC (BIC) for the model i and AIC_s (BIC_s) is the value of AIC (BIC) for the baseline SH0ES model. Note that a positive value of ΔAIC or ΔBIC means a preference for the baseline SH0ES model.

According to the calibrated Jeffreys' scales [175] showed in the Table A2 (see also Refs. [170,174,176–178]), a range of $0 < |\Delta AIC| < 2$ means that the two comparable models have about the same support from the data, a range $4 < |\Delta AIC| < 7$ means this support is considerably less for the model with the larger AIC, while for $|\Delta AIC| > 10$, the model with the larger AIC has no support, i.e., the model is practically irrelevant. Similarly, for two competing models a range $0 < |\Delta BIC| < 2$ is regarded as weak evidence, and a range $2 < |\Delta BIC| < 6$ is regarded as positive evidence, while for $|\Delta BIC| > 6$, the evidence is strong against the model with the larger value.

We attribute the difference between ΔAIC and ΔBIC for the models in consideration of the fact that the BIC penalizes additional parameters more strongly than the AIC as inferred by Equations (A10) and (A11) for the used dataset with $lnN > 2$ (see Refs. [170,171,179].

Appendix E

Here, we present in a comprehensive and concise manner the 3130 Cepheid data that appear in the vector **Y** and in the modeling matrix **L**. The sequence is the same as the one appearing in the top 3130 entries of the vector **Y** released in the form of fits files by R21. Even though no new information is presented in the following Table A3, compared to the released fits files of R21, the concise presentation of these data may make them more useful in various applications and studies.

Table A3. Data for 3130 Cepheids in the host SnIa host galaxies and in the anchor or supporting galaxies N4258, M31, LMC, SMC from fits files in R21. An electronic version of the complete table is available in the A reanalysis of the SH0ES data for H_0 GitHub repository, https://github.com/FOTEINISKARA/A-reanalysis-of-the-SH0ES-data-for-H_0 (accessed on 23 August 2022) under the MIT license.

Galaxy	Ranking in Vector Y	$\bar{m}^W_H$ [mag]	σ [mag]	[P] [dex]	[O/H] [dex]
M1337	1	27.52	0.39	0.45	−0.2
M1337	2	28.05	0.47	0.65	−0.19
M1337	3	26.56	0.35	0.6	−0.2
M1337	4	26.97	0.27	0.78	−0.2
M1337	5	27.01	0.47	0.72	−0.18
M1337	6	26.29	0.5	0.9	−0.17
M1337	7	26.12	0.6	0.89	−0.17
M1337	8	26.94	0.45	0.75	−0.17
M1337	9	27.78	0.61	0.69	−0.16
M1337	10	26.17	0.55	0.7	−0.14
M1337	11	26.63	0.65	0.49	−0.22
M1337	12	27.4	0.39	0.85	−0.19

Table A3. *Cont.*

Galaxy	Ranking in Vector Y	$\bar{m}_H^W$ [mag]	σ [mag]	[P] [dex]	[O/H] [dex]
M1337	13	27.26	0.53	0.52	−0.22
M1337	14	27.34	0.34	0.85	−0.17
M1337	15	27	0.54	0.7	−0.19
N0691	1	26.59	0.57	0.4	0.09
N0691	2	27.1	0.46	0.61	0.06
N0691	3	26.79	0.47	0.71	0.04
N0691	4	26.83	0.5	0.78	0.14
N0691	5	26.23	0.44	0.51	0.05
N0691	6	27.16	0.48	0.63	0.1
N0691	7	26.89	0.46	0.7	0.03
N0691	8	26.75	0.59	0.43	0.03
N0691	9	27.11	0.28	0.88	0.04
N0691	10	26.99	0.68	0.62	0.1
N0691	11	27.6	0.35	0.81	0.07
N0691	12	27.33	0.38	0.75	0.08
N0691	13	26.6	0.53	0.54	0.14
N0691	14	26.34	0.45	0.74	0.09
N0691	15	26.91	0.3	0.96	0.11
N0691	16	26.79	0.49	0.84	0.13
N0691	17	27.08	0.48	0.63	0.1
N0691	18	27.07	0.59	0.63	0.1
N0691	19	26.69	0.63	0.53	0.07
N0691	20	27.94	0.58	0.49	0.11
N0691	21	26.15	0.62	0.48	0.12
N0691	22	26.46	0.43	0.74	0.11
N0691	23	27.16	0.6	0.42	0.14
N0691	24	26.96	0.38	0.8	0.14
N0691	25	26.59	0.44	0.65	0.04
N0691	26	26.61	0.52	0.5	0.09
N0691	27	26.21	0.6	0.62	0.11
N0691	28	27.42	0.65	0.65	0.1
...	...	...	...	...	...

Notes

1 At a distance $D = 7.6Mpc$ [156], NGC 4258 is the closest galaxy, beyond the Local Group with a geometric distance measurement.

2 A differential distance measurement of the SMC with respect to the LMC is used and thus LMC+SMC are considered in a unified manner in the released data.

3 45 Cepheids in N1365 are mentioned in R21 but there are 46 in the fits files of the released dataset at Github repository: PantheonPlusSH0ES/DataRelease (accessed on 25 June 2022).

4 A total of 3130 Cepheids have been released in the data fits files but 3129 are mentioned in R21 (see Table 3). These data are also shown concisely in Table A3 of Appendix E and may be download in electronic form.

5 This parameter is not defined in R21 but is included in the data release fits files. We thank A. Riess for clarifying this point.

6 For Cepheids in the LMC/SMC anchor observed from the ground, the zeropoint parameter zp is added on the RHS, and thus Equation (6) becomes $m^W_{H,i,j} = \mu_i + M^W_{H,i} + b_W[P]_{i,j} + Z_W[O/H]_{i,j} + zp$ to allow for a different P-L zeropoint between ground and HST observations.

7 In the case of SMC, a differential distance with respect to LMC is used.

8 The **Y**, **L** and **C** matrices have been made publicly available as fits files by the SH0ES team at Github repository: PantheonPlusSH0ES/DataRelease (accessed on 25 June 2022).

9 The results for the parameters in $\mathbf{q_{best}}$ are the same as the results obtained using the numerical minimization of χ^2 (see the absolute matching of the results in the numerical analysis file "Baseline1 structure of system" in the A reanalysis of the SH0ES data for H_0 GitHub repository (accessed on 23 August 2022)).

10 We use the standard notation $\log \equiv \log_{10}$ which is important in the error propagation to H_0.

11 37 SnIa/Cepheid hosts and 3 pure Cepheid hosts of which 2 are anchors (N4258 and LMC)

[12] As discussed in Appendix C, two slopes corresponding to the hosts N4038 and N1365 are slightly shifted in our analysis compared to R21 due a small disagreement in the best-fit slope and a typo of R21 in transferring the correct slope to Figure 10, while the slope corresponding to the host N4424 is missing in Figure 10 of R21.

[13] The number of degrees of freedom is $dof = N - M = 42 - 1 = 41$ for b_W and $dof = N - M = 40 - 1 = 39$ for Z_W. The smaller number of N for Z_W is due to the fact that metallicities were not provided for individual Cepheids in the LMC and SMS in R21, and thus, we evaluated a smaller number of slopes for Z_W. See also Table A1. The $N = 42$ points shown in the plot 1 include the two additional points corresponding to MW and SMC (which is degenerate with LMC).

[14] Some hosts have more than one SnIa and more than one light curve and thus, averaging with proper uncertainties was implemented in these cases.

[15] For more details see https://people.duke.edu/~hpgavin/SystemID/CourseNotes/linear-least-squres.pdf (accessed on 28 June 2022).

References

1. Riess, A.G.; Yuan, W.; Macri, L.M.; Scolnic, D.; Brout, D.; Casertano, S.; Jones, D.O.; Murakami, Y.; Anand, G.S.; Breuval, L.; et al. A Comprehensive Measurement of the Local Value of the Hubble Constant with 1 km s^{-1} Mpc^{-1} Uncertainty from the Hubble Space Telescope and the SH0ES Team. *Astrophys. J. Lett.* **2022**, *934*, L7. [CrossRef]
2. Freedman, W.L. Measurements of the Hubble Constant: Tensions in Perspective. *arXiv* **2021**, arXiv:2106.15656.
3. Gómez-Valent, A.; Amendola, L. H_0 from cosmic chronometers and Type Ia supernovae, with Gaussian Processes and the novel Weighted Polynomial Regression method. *J. Cosmol. Astropart. Phys.* **2018**, *04*, 051. [CrossRef]
4. Pesce, D.; Braatz, J.A.; Reid, M.J.; Riess, A.G.; Scolnic, D.; Condon, J.J.; Gao, F.; Henkel, C.; Impellizzeri, C.M.V.; Kuo, C.Y.; et al. The Megamaser Cosmology Project. XIII. Combined Hubble constant constraints. *Astrophys. J. Lett.* **2020**, *891*, L1. [CrossRef]
5. Freedman, W.L.; Madore, B.F.; Hoyt, T.; Jang, I.S.; Beaton, R.; Lee, M.G.; Monson, A.; Neeley, J.; Rich, J. Calibration of the Tip of the Red Giant Branch (TRGB). *arXiv* **2020**, arXiv:2002.01550.
6. Wong, K.C.; Suyu, S.H.; Chen, G.C.-F.; E Rusu, C.; Millon, M.; Sluse, D.; Bonvin, V.; Fassnacht, C.D.; Taubenberger, S.; Auger, M.W.; et al. H0LiCOW – XIII. A 2.4 per cent measurement of H0 from lensed quasars: 5.3σ tension between early- and late-Universe probes. *Mon. Not. Roy. Astron. Soc.* **2020**, *498*, 1420–1439. [CrossRef]
7. Chen, G.C.F.; Fassnacht, C.; Suyu, S.H.; E Rusu, C.; Chan, J.H.H.; Wong, K.C.; Auger, M.W.; Hilbert, S.; Bonvin, V.; Birrer, S.; et al. A SHARP view of H0LiCOW: H_0 from three time-delay gravitational lens systems with adaptive optics imaging. *Mon. Not. Roy. Astron. Soc.* **2019**, *490*, 1743–1773. [CrossRef]
8. Birrer, S.; Shajib, A.J.; Galan, A.; Millon, M.; Treu, T.; Agnello, A.; Auger, M.; Chen, G.C.-F.; Christensen, L.; Van de Vyvere, L.; et al. TDCOSMO - IV. Hierarchical time-delay cosmography – joint inference of the Hubble constant and galaxy density profiles. *Astron. Astrophys.* **2020**, *643*, A165, [CrossRef]
9. Birrer, S.; Treu, T.; E Rusu, C.; Bonvin, V.; Fassnacht, C.; Chan, J.H.H.; Agnello, A.; Shajib, A.J.; Chen, G.C.-F.; Auger, M.; et al. H0LiCOW - IX. Cosmographic analysis of the doubly imaged quasar SDSS 1206+4332 and a new measurement of the Hubble constant. *Mon. Not. Roy. Astron. Soc.* **2019**, *484*, 4726. [CrossRef]
10. Fishbach, M.; Gray, R.; Hernandez, I.M.; Qi, H.; Sur, A.; Acernese, F.; Aiello, L.; Allocca, A.; Aloy, M.A.; Amato, A.; et al. A Standard Siren Measurement of the Hubble Constant from GW170817 without the Electromagnetic Counterpart. *Astrophys. J. Lett.* **2019**, *871*, L13. [CrossRef]
11. Hotokezaka, K.; Nakar, E.; Gottlieb, O.; Nissanke, S.; Masuda, K.; Hallinan, G.; Mooley, K.P.; Deller, A.T. A Hubble constant measurement from superluminal motion of the jet in GW170817. *Nature Astron.* **2019**, *3*, 940–944. [CrossRef]
12. Abbott, B.P.; Shajib, A.J.; Galan, A.; Millon, M.; Treu, T.; Agnello, A.; Auger, M.; Chen, G.C.-F.; Christensen, L.; Collett, T.; et al. A gravitational-wave standard siren measurement of the Hubble constant. *Nature* **2017**, *551*, 85–88. [CrossRef]
13. Palmese, A.; Devicente, J.; Pereira, M.E.S.; Annis, J.; Hartley, W.; Herner, K.; Soares-Santos, M.; Crocce, M.; Huterer, D.; Magaña Hernandez, I.; et al. A statistical standard siren measurement of the Hubble constant from the LIGO/Virgo gravitational wave compact object merger GW190814 and Dark Energy Survey galaxies. *Astrophys. J. Lett.* **2020**, *900*, L33. [CrossRef]
14. Soares-Santos, M.; Palmese, A.; Hartley, W.; Annis, J.; Garcia-Bellido, J.; Lahav, O.; Doctor, Z.; Fishbach, M.; Holz, D.E.; Lin, H.; et al. First Measurement of the Hubble Constant from a Dark Standard Siren using the Dark Energy Survey Galaxies and the LIGO/Virgo Binary–Black-hole Merger GW170814. *Astrophys. J. Lett.* **2019**, *876*, L7, [CrossRef]
15. Cao, S.; Dainotti, M.; Ratra, B. Standardizing Platinum Dainotti-correlated gamma-ray bursts, and using them with standardized Amati-correlated gamma-ray bursts to constrain cosmological model parameters. *Mon. Not. Roy. Astron. Soc.* **2022**, *512*, 439–454. [CrossRef]
16. Cao, S.; Dainotti, M.; Ratra, B. Gamma-ray burst data strongly favor the three-parameter fundamental plane (Dainotti) correlation relation over the two-parameter one. *Mon. Not. R. Astron. Soc.* **2022**, *516*, 1386–1405. [CrossRef]
17. Dainotti, M.G.; Sarracino, G.; Capozziello, S. Gamma-Ray Bursts, Supernovae Ia and Baryon Acoustic Oscillations: A binned cosmological analysis. *Publ. Astron. Soc. Jpn.* **2022**, 74, 1095–1113. [CrossRef]
18. Dainotti, M.G.; Nielson, V.; Sarracino, G.; Rinaldi, E.; Nagataki, S.; Capozziello, S.; Gnedin, O.Y.; Bargiacchi, G. Optical and X-ray GRB Fundamental Planes as cosmological distance indicators. *Mon. Not. Roy. Astron. Soc.* **2022**, *514*, 1828–1856. [CrossRef]
19. Dainotti, M.G.; Cardone, V.F.; Piedipalumbo, E.; Capozziello, S. Slope evolution of GRB correlations and cosmology. *Mon. Not. Roy. Astron. Soc.* **2013**, *436*, 82. [CrossRef]

20. Risaliti, G.; Lusso, E. Cosmological constraints from the Hubble diagram of quasars at high redshifts. *Nat. Astron.* **2019**, *3*, 272–277. [CrossRef]
21. de Jaeger, T.; Galbany, L.; Riess, A.G.; Stahl, B.E.; Shappee, B.J.; Filippenko, A.V.; Zheng, W. A 5% measurement of the Hubble constant from Type II supernovae. *Mon. Not. R. Astron. Soc.* **2020**, *514*, 4620–4628. [CrossRef]
22. de Jaeger, T.; Stahl, B.; Zheng, W.; Filippenko, A.; Riess, A.; Galbany, L. A measurement of the Hubble constant from Type II supernovae. *Mon. Not. R. Astron. Soc.* **2020**, *496*, 3402–3411. [CrossRef]
23. Domínguez, A.; Wojtak, R.; Finke, J.; Ajello, M.; Helgason, K.; Prada, F.; Desai, A.; Paliya, V.; Marcotulli, L.; Hartmann, D. A new measurement of the Hubble constant and matter content of the Universe using extragalactic background light γ-ray attenuation. *Astrophys. J.* **2019**, *885*, 137. [CrossRef]
24. Di Valentino, E.; Mena, O.; Pan, S.; Visinelli, L.; Yang, W.; Melchiorri, A.; Mota, D.F.; Riess, A.G.; Silk, J. In the realm of the Hubble tension—a review of solutions. *Class. Quant. Grav.* **2021**, *38*, 153001. [CrossRef]
25. Perivolaropoulos, L.; Skara, F. Challenges for ΛCDM: An update. *New Astron. Rev.* **2022**, *95*, 101659. [CrossRef]
26. Aghanim, N.; Akrami, Y.; Ashdown, M.; Aumont, J.; Baccigalupi, C.; Ballardini, M.; Banday, A.I.; Barreiro, R.B.; Bartolo, N.; Basak, S.; et al. Planck 2018 results. VI. Cosmological parameters. *Astron. Astrophys.* **2020**, *641*, A6. Erratum *Astron. Astrophys.* **2021**, *652*, C4. [CrossRef]
27. Abdalla, E.; Abellán, G.F.; Aboubrahim, A.; Agnello, A.; Akarsu, O.; Akrami, Y.; Alestas, G.; Aloni, D.; Amendola, L.; Anchordoqui, L.A.; et al. Cosmology intertwined: A review of the particle physics, astrophysics, and cosmology associated with the cosmological tensions and anomalies. *JHEAp* **2022**, *34*, 49–211. [CrossRef]
28. Shah, P.; Lemos, P.; Lahav, O. A buyer's guide to the Hubble constant. *Astron. Astrophys. Rev.* **2021**, *29*, 9. [CrossRef]
29. Knox, L.; Millea, M. The Hubble Hunter's Guide. *arXiv* **2019**, arXiv:1908.03663.
30. Vagnozzi, S. New physics in light of the H_0 tension: An alternative view. *Phys. Rev. D* **2020**, *102*, 023518. [CrossRef]
31. Ishak, M. Testing General Relativity in Cosmology. *Living Rev. Rel.* **2019**, *22*, 1. [CrossRef] [PubMed]
32. Mörtsell, E.; Dhawan, S. Does the Hubble constant tension call for new physics? *JCAP* **2018**, *1809*, 025. [CrossRef]
33. Huterer, D.; Shafer, D.L. Dark energy two decades after: Observables, probes, consistency tests. *Rept. Prog. Phys.* **2018**, *81*, 016901. [CrossRef]
34. Bernal, J.L.; Verde, L.; Riess, A.G. The trouble with H_0. *JCAP* **2016**, *1610*, 019. [CrossRef]
35. Alam, S.; Aubert, M.; Avila, S.; Balland, C.; Bautista, J.E.; Bershady, M.A.; Bizyaev, D.; Blanton, M.R.; Bolton, A.S.; Bovy, J.; et al. Completed SDSS-IV extended Baryon Oscillation Spectroscopic Survey: Cosmological implications from two decades of spectroscopic surveys at the Apache Point Observatory. *Phys. Rev. D* **2021**, *103*, 083533. [CrossRef]
36. Verde, L.; Treu, T.; Riess, A.G. Tensions between the Early and the Late Universe. *Nature Astron.* **2019**, *3*, 891. [CrossRef]
37. Schöneberg, N.; Franco Abellán, G.; Pérez Sánchez, A.; Witte, S.J.; Poulin, V.; Lesgourgues, J. The H_0 Olympics: A fair ranking of proposed models. *arXiv* **2021**, arXiv:2107.10291.
38. Krishnan, C.; Colgáin, E.O.; Ruchika; Sen, A.A.; Sheikh-Jabbari, M.M.; Yang, T. Is there an early Universe solution to Hubble tension? *Phys. Rev. D* **2020**, *102*, 103525. [CrossRef]
39. Jedamzik, K.; Pogosian, L.; Zhao, G.B. Why reducing the cosmic sound horizon can not fully resolve the Hubble tension. *arXiv* **2020**, arXiv:2010.04158.
40. Poulin, V.; Smith, T.L.; Karwal, T.; Kamionkowski, M. Early Dark Energy Can Resolve The Hubble Tension. *Phys. Rev. Lett.* **2019**, *122*, 221301. [CrossRef]
41. Niedermann, F.; Sloth, M.S. New early dark energy. *Phys. Rev. D* **2021**, *103*, L041303. [CrossRef]
42. Smith, T.L.; Lucca, M.; Poulin, V.; Abellan, G.F.; Balkenhol, L.; Benabed, K.; Galli, S.; Murgia, R. Hints of Early Dark Energy in Planck, SPT, and ACT data: New physics or systematics? *arXiv* **2022**, arXiv:2202.09379.
43. Smith, T.L.; Poulin, V.; Bernal, J.L.; Boddy, K.K.; Kamionkowski, M.; Murgia, R. Early dark energy is not excluded by current large-scale structure data. *arXiv* **2020**, arXiv:2009.10740.
44. Chudaykin, A.; Gorbunov, D.; Nedelko, N. Combined analysis of Planck and SPTPol data favors the early dark energy models. *J. Cosmol. Astropart. Phys.* **2020**, *08*, 013. [CrossRef]
45. Fondi, E.; Melchiorri, A.; Pagano, L. No evidence for EDE from Planck data in extended scenarios. *Astrophys. J. Lett.* **2022**, *931*, L18.
46. Sabla, V.I.; Caldwell, R.R. The Microphysics of Early Dark Energy. *arXiv* **2022**, arXiv:2202.08291.
47. Herold, L.; Ferreira, E.G.M.; Komatsu, E. New Constraint on Early Dark Energy from Planck and BOSS Data Using the Profile Likelihood. *Astrophys. J. Lett.* **2022**, *929*, L16. [CrossRef]
48. McDonough, E.; Lin, M.X.; Hill, J.C.; Hu, W.; Zhou, S. Early dark sector, the Hubble tension, and the swampland. *Phys. Rev. D* **2022**, *106*, 043525. [CrossRef]
49. Hill, J.C.; McDonough, E.; Toomey, M.W.; Alexander, S. Early Dark Energy Does Not Restore Cosmological Concordance. *arXiv* **2020**, arXiv:2003.07355.
50. Sakstein, J.; Trodden, M. Early Dark Energy from Massive Neutrinos as a Natural Resolution of the Hubble Tension. *Phys. Rev. Lett.* **2020**, *124*, 161301. [CrossRef]
51. Niedermann, F.; Sloth, M.S. New Early Dark Energy is compatible with current LSS data. *arXiv* **2020**, arXiv:2009.00006.
52. Rezazadeh, K.; Ashoorioon, A.; Grin, D. Cascading Dark Energy. *arXiv* **2022**, arXiv:2208.07631.

53. Green, D.; Amin, M.A.; Meyers, J.; Wallisch, B.; Abazajian, K.N.; Abidi, M.; Adshead, P.; Ahmed, Z.; Ansarinejad, B.; Armstrong, R.; et al. Messengers from the Early Universe: Cosmic Neutrinos and Other Light Relics. *Bull. Am. Astron. Soc.* **2019**, *51*, 159.
54. Schöneberg, N.; Franco Abellán, G. A step in the right direction? Analyzing the Wess Zumino Dark Radiation solution to the Hubble tension. *arXiv* **2022**, arXiv:2206.11276.
55. Seto, O.; Toda, Y. Comparing early dark energy and extra radiation solutions to the Hubble tension with BBN. *arXiv* **2021**, arXiv:2101.03740.
56. Carrillo González, M.; Liang, Q.; Sakstein, J.; Trodden, M. Neutrino-Assisted Early Dark Energy: Theory and Cosmology. *arXiv* **2020**, arXiv:2011.09895.
57. Braglia, M.; Ballardini, M.; Finelli, F.; Koyama, K. Early modified gravity in light of the H_0 tension and LSS data. *Phys. Rev. D* **2021**, *103*, 043528. [CrossRef]
58. Abadi, T.; Kovetz, E.D. Can conformally coupled modified gravity solve the Hubble tension? *Phys. Rev. D* **2021**, *103*, 023530. [CrossRef]
59. Renk, J.; Zumalacárregui, M.; Montanari, F.; Barreira, A. Galileon gravity in light of ISW, CMB, BAO and H_0 data. *J. Cosmol. Astropart. Phys.* **2017**, *1710*, 020. [CrossRef]
60. Nojiri, S.; Odintsov, S.D.; Oikonomou, V.K. Integral F(R) gravity and saddle point condition as a remedy for the H0-tension. *Nucl. Phys. B* **2022**, *980*, 115850. [CrossRef]
61. Lin, M.X.; Raveri, M.; Hu, W. Phenomenology of Modified Gravity at Recombination. *Phys. Rev.* **2019**, *D99*, 043514. [CrossRef]
62. Saridakis, E.N.; Lazkoz, R.; Salzano, V.; Moniz, P.V.; Capozziello, S.; Jiménez, J.B.; De Laurentis, M.; Olmo, G.J. Modified Gravity and Cosmology: An Update by the CANTATA Network. *arXiv* **2021**, arXiv:2105.12582.
63. Benisty, D. Quantifying the S_8 tension with the Redshift Space Distortion data set. *Phys. Dark Univ.* **2021**, *31*, 100766. [CrossRef]
64. Heymans, C.; Tröster, T.; Asgari, M.; Blake, C.; Hildebrandt, H.; Joachimi, B.; Kuijken, K.; Lin, C.-A.; Sánchez, A.G.; Busch, J.L.V.D.; et al. KiDS-1000 Cosmology: Multi-probe weak gravitational lensing and spectroscopic galaxy clustering constraints. *Astron. Astrophys.* **2021**, *646*, A140. [CrossRef]
65. Kazantzidis, L.; Perivolaropoulos, L. Evolution of the $f\sigma_8$ tension with the Planck15/ΛCDM determination and implications for modified gravity theories. *Phys. Rev. D* **2018**, *97*, 103503, [CrossRef]
66. Joudaki, S.; Blake, C.; Johnson, A.; Amon, A.; Asgari, M.; Choi, A.; Erben, T.; Glazebrook, K.; Harnois-Déraps, J.; Heymans, C.; et al. KiDS-450 + 2dFLenS: Cosmological parameter constraints from weak gravitational lensing tomography and overlapping redshift-space galaxy clustering. *Mon. Not. Roy. Astron. Soc.* **2018**, *474*, 4894–4924. [CrossRef]
67. Kazantzidis, L.; Perivolaropoulos, L. σ_8 Tension. Is Gravity Getting Weaker at Low z? Observational Evidence and Theoretical Implications. In *Modified Gravity and Cosmology*; Springer: Cham, Switzerland, 2019; pp. 507–537. [CrossRef]
68. Skara, F.; Perivolaropoulos, L. Tension of the E_G statistic and redshift space distortion data with the Planck - ΛCDM model and implications for weakening gravity. *Phys. Rev. D* **2020**, *101*, 063521. [CrossRef]
69. Avila, F.; Bernui, A.; Bonilla, A.; Nunes, R.C. Inferring $S_8(z)$ and $\gamma(z)$ with cosmic growth rate measurements using machine learning. *Eur. Phys. J. C* **2022**, *82*, 594. [CrossRef]
70. Köhlinger, F.; Viola, M.; Joachimi, B.; Hoekstra, H.; Van Uitert, E.; Hildebrandt, H.; Choi, A.; Erben, T.; Heymans, C.; Joudaki, S.; et al. KiDS-450: The tomographic weak lensing power spectrum and constraints on cosmological parameters. *Mon. Not. Roy. Astron. Soc.* **2017**, *471*, 4412–4435. [CrossRef]
71. Nunes, R.C.; Vagnozzi, S. Arbitrating the S8 discrepancy with growth rate measurements from redshift-space distortions. *Mon. Not. Roy. Astron. Soc.* **2021**, *505*, 5427–5437. [CrossRef]
72. Clark, S.J.; Vattis, K.; Fan, J.; Koushiappas, S.M. The H_0 and S_8 tensions necessitate early and late time changes to ΛCDM. *arXiv* **2021**, arXiv:2110.09562.
73. Ivanov, M.M.; McDonough, E.; Hill, J.C.; Simonović, M.; Toomey, M.W.; Alexander, S.; Zaldarriaga, M. Constraining Early Dark Energy with Large-Scale Structure. *Phys. Rev. D* **2020**, *102*, 103502. [CrossRef]
74. Hill, J.C.; Calabrese, E.; Aiola, S.; Battaglia, N.; Bolliet, B.; Choi, S.K.; Devlin, M.J.; Duivenvoorden, A.J.; Dunkley, J.; Ferraro, S.; et al. Atacama Cosmology Telescope: Constraints on prerecombination early dark energy. *Phys. Rev. D* **2022**, *105*, 123536. [CrossRef]
75. Vagnozzi, S. Consistency tests of ΛCDM from the early integrated Sachs-Wolfe effect: Implications for early-time new physics and the Hubble tension. *Phys. Rev. D* **2021**, *104*, 063524. [CrossRef]
76. Philcox, O.H.E.; Farren, G.S.; Sherwin, B.D.; Baxter, E.J.; Brout, D.J. Determining the Hubble Constant without the Sound Horizon: A 3.6% Constraint on H_0 from Galaxy Surveys, CMB Lensing and Supernovae. *arXiv* **2022**, arXiv:2204.02984.
77. Chudaykin, A.; Gorbunov, D.; Nedelko, N. Exploring an early dark energy solution to the Hubble tension with Planck and SPTPol data. *Phys. Rev. D* **2021**, *103*, 043529. [CrossRef]
78. Reeves, A.; Herold, L.; Vagnozzi, S.; Sherwin, B.D.; Ferreira, E.G.M. Restoring cosmological concordance with early dark energy and massive neutrinos? *arXiv* **2022**, arXiv:2207.01501.
79. Solà Peracaula, J.; Gómez-Valent, A.; de Cruz Pérez, J.; Moreno-Pulido, C. Brans–Dicke cosmology with a Λ-term: A possible solution to ΛCDM tensions. *Class. Quant. Grav.* **2020**, *37*, 245003. [CrossRef]
80. Braglia, M.; Ballardini, M.; Emond, W.T.; Finelli, F.; Gumrukcuoglu, A.E.; Koyama, K.; Paoletti, D. Larger value for H_0 by an evolving gravitational constant. *Phys. Rev. D* **2020**, *102*, 023529. [CrossRef]

81. Pogosian, L.; Raveri, M.; Koyama, K.; Martinelli, M.; Silvestri, A.; Zhao, G.B. Imprints of cosmological tensions in reconstructed gravity. *arXiv* **2021**, arXiv:2107.12992.
82. Bahamonde, S.; Dialektopoulos, K.F.; Escamilla-Rivera, C.; Farrugia, G.; Gakis, V.; Hendry, M.; Hohmann, M.; Said, J.L.; Mifsud, J.; Di Valentino, E. Teleparallel Gravity: From Theory to Cosmology. *arXiv* **2021**, arXiv:2106.13793.
83. Di Valentino, E.; Mukherjee, A.; Sen, A.A. Dark Energy with Phantom Crossing and the H_0 Tension. *Entropy* **2021**, *23*, 404. [CrossRef] [PubMed]
84. Alestas, G.; Kazantzidis, L.; Perivolaropoulos, L. H_0 Tension, Phantom Dark Energy and Cosmological Parameter Degeneracies. *Phys. Rev. D* **2020**, *101*, 123516. [CrossRef]
85. Di Valentino, E.; Melchiorri, A.; Mena, O.; Vagnozzi, S. Nonminimal dark sector physics and cosmological tensions. *Phys. Rev. D* **2020**, *101*, 063502. [CrossRef]
86. Pan, S.; Yang, W.; Di Valentino, E.; Shafieloo, A.; Chakraborty, S. Reconciling H_0 tension in a six parameter space? *J. Cosmol. Astropart. Phys.* **2020**, *06*, 062, [CrossRef]
87. Li, X.; Shafieloo, A. A Simple Phenomenological Emergent Dark Energy Model can Resolve the Hubble Tension. *Astrophys. J. Lett.* **2019**, *883*, L3. [CrossRef]
88. Zhao, G.B.; Raveri, M.; Pogosian, L.; Wang, Y.; Crittenden, R.G.; Handley, W.; Percival, W.J.; Beutler, F.; Brinkmann, J.; Chuang, C.-H.; et al. Dynamical dark energy in light of the latest observations. *Nature Astron.* **2017**, *1*, 627–632. [CrossRef]
89. Keeley, R.E.; Joudaki, S.; Kaplinghat, M.; Kirkby, D. Implications of a transition in the dark energy equation of state for the H_0 and σ_8 tensions. *J. Cosmol. Astropart. Phys.* **2019**, *12*, 035. [CrossRef]
90. Sola Peracaula, J.; Gomez-Valent, A.; de Cruz Pérez, J. Signs of Dynamical Dark Energy in Current Observations. *Phys. Dark Univ.* **2019**, *25*, 100311. [CrossRef]
91. Yang, W.; Pan, S.; Di Valentino, E.; Saridakis, E.N.; Chakraborty, S. Observational constraints on one-parameter dynamical dark-energy parametrizations and the H_0 tension. *Phys. Rev.* **2019**, *D99*, 043543. [CrossRef]
92. Krishnan, C.; Colgáin, E.O.; Sheikh-Jabbari, M.M.; Yang, T. Running Hubble Tension and a H0 Diagnostic. *Phys. Rev. D* **2021**, *103*, 103509. [CrossRef]
93. Dainotti, M.G.; De Simone, B.; Schiavone, T.; Montani, G.; Rinaldi, E.; Lambiase, G. On the Hubble constant tension in the SNe Ia Pantheon sample. *Astrophys. J.* **2021**, *912*, 150. [CrossRef]
94. Colgáin, E.O.; Sheikh-Jabbari, M.M.; Solomon, R.; Bargiacchi, G.; Capozziello, S.; Dainotti, M.G.; Stojkovic, D. Revealing intrinsic flat ΛCDM biases with standardizable candles. *Phys. Rev. D* **2022**, *106*, L041301. [CrossRef]
95. Colgáin, E.O.; Sheikh-Jabbari, M.M.; Solomon, R.; Dainotti, M.G.; Stojkovic, D. Putting Flat ΛCDM In The (Redshift) Bin. *arXiv* **2022**, arXiv:2206.11447.
96. Zhou, Z.; Liu, G.; Xu, L. Can late dark energy restore the Cosmic concordance? *arXiv* **2021**, arXiv:2105.04258.
97. Di Valentino, E.; Melchiorri, A.; Mena, O.; Vagnozzi, S. Interacting dark energy in the early 2020s: A promising solution to the H_0 and cosmic shear tensions. *Phys. Dark Univ.* **2020**, *30*, 100666. [CrossRef]
98. Yang, W.; Pan, S.; Di Valentino, E.; Nunes, R.C.; Vagnozzi, S.; Mota, D.F. Tale of stable interacting dark energy, observational signatures, and the H_0 tension. *J. Cosmol. Astropart. Phys.* **2018**, *1809*, 019, [CrossRef]
99. Vattis, K.; Koushiappas, S.M.; Loeb, A. Dark matter decaying in the late Universe can relieve the H0 tension. *Phys. Rev.* **2019**, *D99*, 121302. [CrossRef]
100. Yang, W.; Mukherjee, A.; Di Valentino, E.; Pan, S. Interacting dark energy with time varying equation of state and the H_0 tension. *Phys. Rev.* **2018**, *D98*, 123527. [CrossRef]
101. Ghosh, S.; Khatri, R.; Roy, T.S. Can dark neutrino interactions phase out the Hubble tension? *Phys. Rev. D* **2020**, *102*, 123544. [CrossRef]
102. Brieden, S.; Gil-Marín, H.; Verde, L. Model-agnostic interpretation of 10 billion years of cosmic evolution traced by BOSS and eBOSS data. *J. Cosmol. Astropart. Phys.* **2022**, *08*, 024, [CrossRef]
103. Alestas, G.; Perivolaropoulos, L. Late time approaches to the Hubble tension deforming $H(z)$, worsen the growth tension. *Mon. Not. Roy. Astron. Soc.* **2021**, *504*, 3956. [CrossRef]
104. Keeley, R.E.; Shafieloo, A. Ruling Out New Physics at Low Redshift as a solution to the H_0 Tension. *arXiv* **2022**, arXiv:2206.08440.
105. Clark, S.J.; Vattis, K.; Koushiappas, S.M. CMB constraints on late-universe decaying dark matter as a solution to the H_0 tension. *arXiv* **2020**, arXiv:2006.03678.
106. Chen, A.; Huterer, D.; Lee, S.; Ferté, A.; Weaverdyck, N.; Alves, O.; Leonard, C.D.; MacCrann, N.; Raveri, M.; Porredon, A.; et al. Constraints on dark matter to dark radiation conversion in the late universe with DES-Y1 and external data. *Phys. Rev. D* **2021**, *103*, 123528. [CrossRef]
107. Anchordoqui, L.A.; Barger, V.; Marfatia, D.; Soriano, J.F. Decay of multiple dark matter particles to dark radiation in different epochs does not alleviate the Hubble tension. *Phys. Rev. D* **2022**, *105*, 103512. [CrossRef]
108. Mau, S.; Nadler, E.O.; Wechsler, R.H.; Drlica-Wagner, A.; Bechtol, K.; Green, G.; Huterer, D.; Li, T.S.; Mao, Y.-Y.; Martínez-Vázquez, C.E.; et al. Milky Way Satellite Census. IV. Constraints on Decaying Dark Matter from Observations of Milky Way Satellite Galaxies. *Astrophys. J.* **2022**, *932*, 128. [CrossRef]
109. Cai, R.G.; Guo, Z.K.; Wang, S.J.; Yu, W.W.; Zhou, Y. No-go guide for the Hubble tension: Matter perturbations. *arXiv* **2020**, arXiv:2202.12214.

110. Heisenberg, L.; Villarrubia-Rojo, H.; Zosso, J. Can late-time extensions solve the H0 and σ8 tensions? *Phys. Rev. D* **2022**, *106*, 043503. [CrossRef]
111. Vagnozzi, S.; Pacucci, F.; Loeb, A. Implications for the Hubble tension from the ages of the oldest astrophysical objects. *JHEAp* **2022**, *36*, 27–35. [CrossRef]
112. Davari, Z.; Khosravi, N. Can decaying dark matter scenarios alleviate both H_0 and σ_8 tensions? *arXiv* **2020**, arXiv:2203.09439.
113. Mortsell, E.; Goobar, A.; Johansson, J.; Dhawan, S. The Hubble Tension Bites the Dust: Sensitivity of the Hubble Constant Determination to Cepheid Color Calibration. *arXiv* **2021**, arXiv:2105.11461.
114. Efstathiou, G. H0 Revisited. *Mon. Not. Roy. Astron. Soc.* **2014**, *440*, 1138–1152. [CrossRef]
115. Efstathiou, G. A Lockdown Perspective on the Hubble Tension (with comments from the SH0ES team). *arXiv* **2020**, arXiv:2007.10716.
116. Efstathiou, G. To H0 or not to H0? *arXiv* **2021**, arXiv:2103.08723.
117. Wojtak, R.; Hjorth, J. Intrinsic tension in the supernova sector of the local Hubble constant measurement and its implications. *arXiv* **2022**, arXiv:2206.08160. https://doi.org/10.1093/mnras/stac1878.
118. Benisty, D.; Mifsud, J.; Said, J.L.; Staicova, D. On the Robustness of the Constancy of the Supernova Absolute Magnitude: Non-parametric Reconstruction & Bayesian approaches. *arXiv* **2022**, arXiv:2202.04677.
119. Martinelli, M.; Tutusaus, I. CMB tensions with low-redshift H_0 and S_8 measurements: Impact of a redshift-dependent type-Ia supernovae intrinsic luminosity. *Symmetry* **2019**, *11*, 986. [CrossRef]
120. Tinsley, B.M. Evolution of the Stars and Gas in Galaxies. *Astroph. J.* **1968**, *151*, 547. [CrossRef]
121. Kang, Y.; Lee, Y.W.; Kim, Y.L.; Chung, C.; Ree, C.H. Early-type Host Galaxies of Type Ia Supernovae. II. Evidence for Luminosity Evolution in Supernova Cosmology. *Astrophys. J.* **2020**, *889*, 8. [CrossRef]
122. Rose, B.M.; Garnavich, P.M.; Berg, M.A. Think Global, Act Local: The Influence of Environment Age and Host Mass on Type Ia Supernova Light Curves. *Astrophys. J.* **2019**, *874*, 32. [CrossRef]
123. Jones, D.O.; Riess, A.G.; Scolnic, D.M.; Pan, Y.-C.; Johnson, E.; Coulter, D.A.; Dettman, K.; Foley, M.; Foley, R.J.; Huber, M.E.; et al. Should Type Ia Supernova Distances be Corrected for their Local Environments? *Astrophys. J.* **2018**, *867*, 108. [CrossRef]
124. Rigault, M.; Brinnel, V.; Aldering, G.; Antilogus, P.; Aragon, C.; Bailey, S.; Baltay, C.; Barbary, K.; Bongard, S.; Boone, K.; et al. Strong Dependence of Type Ia Supernova Standardization on the Local Specific Star Formation Rate. *Astron. Astrophys.* **2020**, *644*, A176. [CrossRef]
125. Kim, Y.L.; Smith, M.; Sullivan, M.; Lee, Y.W. Environmental Dependence of Type Ia Supernova Luminosities from a Sample without a Local-Global Difference in Host Star Formation. *Astroph. J.* **2018**, *854*, 24. [CrossRef]
126. Colgáin, E.O. A hint of matter underdensity at low z? *J. Cosmol. Astropart. Phys.* **2019**, *09*, 006. [CrossRef]
127. Kazantzidis, L.; Perivolaropoulos, L. Hints of a Local Matter Underdensity or Modified Gravity in the Low z Pantheon data. *Phys. Rev. D* **2020**, *102*, 023520. [CrossRef]
128. Sapone, D.; Nesseris, S.; Bengaly, C.A.P. Is there any measurable redshift dependence on the SN Ia absolute magnitude? *Phys. Dark Univ.* **2021**, *32*, 100814. [CrossRef]
129. Koo, H.; Shafieloo, A.; Keeley, R.E.; L'Huillier, B. Model-independent Constraints on Type Ia Supernova Light-curve Hyperparameters and Reconstructions of the Expansion History of the Universe. *Astrophys. J.* **2020**, *899*, 9. [CrossRef]
130. Kazantzidis, L.; Koo, H.; Nesseris, S.; Perivolaropoulos, L.; Shafieloo, A. Hints for possible low redshift oscillation around the best-fitting ΛCDM model in the expansion history of the Universe. *Mon. Not. Roy. Astron. Soc.* **2021**, *501*, 3421–3426. [CrossRef]
131. Luković, V.V.; Haridasu, B.S.; Vittorio, N. Exploring the evidence for a large local void with supernovae Ia data. *Mon. Not. Roy. Astron. Soc.* **2020**, *491*, 2075–2087. [CrossRef]
132. Tutusaus, I.; Lamine, B.; Blanchard, A. Model-independent cosmic acceleration and redshift-dependent intrinsic luminosity in type-Ia supernovae. *Astron. Astrophys.* **2019**, *625*, A15. [CrossRef]
133. Tutusaus, I.; Lamine, B.; Dupays, A.; Blanchard, A. Is cosmic acceleration proven by local cosmological probes? *Astron. Astrophys.* **2017**, *602*, A73. [CrossRef]
134. Drell, P.S.; Loredo, T.J.; Wasserman, I. Type Ia supernovae, evolution, and the cosmological constant. *Astrophys. J.* **2000**, *530*, 593. [CrossRef]
135. Kenworthy, W.D.; Scolnic, D.; Riess, A. The Local Perspective on the Hubble Tension: Local Structure Does Not Impact Measurement of the Hubble Constant. *Astrophys. J.* **2019**, *875*, 145. [CrossRef]
136. Riess, A.G.; Breuval, L.; Yuan, W.; Casertano, S.; ~Macri, L.M.; Scolnic, D.; Cantat-Gaudin, T.; Anderson, R.I.; Reyes, M.C. Cluster Cepheids with High Precision Gaia Parallaxes, Low Zeropoint Uncertainties, and Hubble Space Telescope Photometry. *arXiv* **2022**, arXiv:2208.01045.
137. Yuan, W.; Macri, L.M.; Riess, A.G.; Brink, T.G.; Casertano, S.; Filippenko, A.V.; Hoffmann, S.L.; Huang, C.D.; Scolnic, D. Absolute Calibration of Cepheid Period-Luminosity Relations in NGC 4258. *arXiv* **2022**, arXiv:2203.06681.
138. Riess, A.G.; Casertano, S.; Yuan, W.; Macri, L.; Bucciarelli, B.; Lattanzi, M.G.; MacKenty, J.W.; Bowers, J.B.; Zheng, W.; Filippenko, A.V.; et al. Milky Way Cepheid Standards for Measuring Cosmic Distances and Application to Gaia DR2: Implications for the Hubble Constant. *Astrophys. J.* **2018**, *861*, 126. [CrossRef]
139. Dainotti, M.G.; De Simone, B.; Schiavone, T.; Montani, G.; Rinaldi, E.; Lambiase, G.; Bogdan, M.; Ugale, S. On the Evolution of the Hubble Constant with the SNe Ia Pantheon Sample and Baryon Acoustic Oscillations: A Feasibility Study for GRB-Cosmology in 2030. *Galaxies* **2022**, *10*, 24. [CrossRef]

140. Bargiacchi, G.; Benetti, M.; Capozziello, S.; Lusso, E.; Risaliti, G.; Signorini, M. Quasar cosmology: Dark energy evolution and spatial curvature. *arXiv* **2021**, arXiv:2111.02420.
141. Dainotti, M.G.; Bardiacchi, G.; Lenart, A.L.; Capozziello, S.; Colgain, E.O.; Solomon, R.; Stojkovic, D.; Sheikh-Jabbari, M.M. Quasar Standardization: Overcoming Selection Biases and Redshift Evolution. *Astrophys. J.* **2022**, *931*, 106. [CrossRef]
142. Khosravi, N.; Farhang, M. Phenomenological gravitational phase transition: Early and late modifications. *Phys. Rev. D* **2022**, *105*, 063505. [CrossRef]
143. Perivolaropoulos, L.; Skara, F. Gravitational transitions via the explicitly broken symmetron screening mechanism. *arXiv* **2022**, arXiv:2203.10374.
144. Alestas, G.; Camarena, D.; Di Valentino, E.; Kazantzidis, L.; Marra, V.; Nesseris, S.; Perivolaropoulos, L. Late-transition versus smooth H(z)-deformation models for the resolution of the Hubble crisis. *Phys. Rev. D* **2022**, *105*, 063538. [CrossRef]
145. Desmond, H.; Jain, B.; Sakstein, J. Local resolution of the Hubble tension: The impact of screened fifth forces on the cosmic distance ladder. *Phys. Rev.* **2019**, *D100*, 043537. [CrossRef]
146. Perivolaropoulos, L.; Skara, F. Hubble tension or a transition of the Cepheid SnIa calibrator parameters? *Phys. Rev. D* **2021**, *104*, 123511. [CrossRef]
147. Odintsov, S.D.; Oikonomou, V.K. Did the Universe experience a pressure non-crushing type cosmological singularity in the recent past? *Europhys. Lett.* **2022**, *137*, 39001. [CrossRef]
148. Alestas, G.; Kazantzidis, L.; Perivolaropoulos, L. $w - M$ phantom transition at $z_t < 0.1$ as a resolution of the Hubble tension. *Phys. Rev. D* **2021**, *103*, 083517. [CrossRef]
149. Marra, V.; Perivolaropoulos, L. A rapid transition of $G_{\rm eff}$ at $z_t \simeq 0.01$ as a possible solution of the Hubble and growth tensions. *Phys. Rev. D* **2021**, *104*, L021303. [CrossRef]
150. Alestas, G.; Antoniou, I.; Perivolaropoulos, L. Hints for a gravitational constant transition in Tully-Fisher data. *arXiv* **2021**, arXiv:2104.14481.
151. Perivolaropoulos, L. Is the Hubble Crisis Connected with the Extinction of Dinosaurs? *Universe* **2022**, *8*, 263. [CrossRef]
152. Odintsov, S.D.; Oikonomou, V.K. Dissimilar donuts in the sky? Effects of a pressure singularity on the circular photon orbits and shadow of a cosmological black hole. *Europhys. Lett.* **2022**, *139*, 59003. [CrossRef]
153. Riess, A.G.; Macri, L.; Hoffmann, S.L.; Scolnic, D.; Casertano, S.; Filippenko, A.V.; Tucker, B.E.; Reid, M.J.; Jones, D.O.; Silverman, J.M.; et al. A 2.4% Determination of the Local Value of the Hubble Constant. *Astrophys. J.* **2016**, *826*, 56. [CrossRef]
154. Riess, A.G.; Casertano, S.; Yuan, W.; Macri, L.M.; Scolnic, D. Large Magellanic Cloud Cepheid Standards Provide a 1% Foundation for the Determination of the Hubble Constant and Stronger Evidence for Physics beyond ΛCDM. *Astrophys. J.* **2019**, *876*, 85. [CrossRef]
155. Riess, A.G.; Casertano, S.; Yuan, W.; Bowers, J.B.; Macri, L.; Zinn, J.C.; Scolnic, D. Cosmic Distances Calibrated to 1% Precision with Gaia EDR3 Parallaxes and Hubble Space Telescope Photometry of 75 Milky Way Cepheids Confirm Tension with ΛCDM. *Astrophys. J. Lett.* **2021**, *908*, L6. [CrossRef]
156. Reid, M.; Pesce, D.; Riess, A. An Improved Distance to NGC 4258 and its Implications for the Hubble Constant. *Astrophys. J. Lett.* **2019**, *886*, L27. [CrossRef]
157. Li, S.; Riess, A.G.; Busch, M.P.; Casertano, S.; Macri, L.M.; Yuan, W. A sub-2% Distance to M31 from Photometrically Homogeneous Near-Infrared Cepheid Period-Luminosity Relations Measured with the Hubble Space Telescope. *arXiv* **2021**, arXiv:2107.08029.
158. Madore, B.F. The period-luminosity relation. IV. Intrinsic relations and reddenings for the Large Magellanic Cloud Cepheids. *Astroph. J.* **1982**, *253*, 575–579. [CrossRef]
159. Fitzpatrick, E.L. Correcting for the effects of interstellar extinction. *Publ. Astron. Soc. Pac.* **1999**, *111*, 63–75. [CrossRef]
160. Camarena, D.; Marra, V. On the use of the local prior on the absolute magnitude of Type Ia supernovae in cosmological inference. *Mon. Not. Roy. Astron. Soc.* **2021**, *504*, 5164–5171. [CrossRef]
161. Gómez-Valent, A. Measuring the sound horizon and absolute magnitude of SNIa by maximizing the consistency between low-redshift data sets. *Phys. Rev. D* **2022**, *105*, 043528. [CrossRef]
162. Kerscher, M.; Weller, J. On Model Selection in Cosmology. *SciPost Phys. Lect. Notes* **2019**, *9*, 1. [CrossRef]
163. Liddle, A.R. Information criteria for astrophysical model selection. *Mon. Not. Roy. Astron. Soc.* **2007**, *377*, L74–L78. [CrossRef]
164. Akaike, H. A new look at the statistical model identification. *IEEE Trans. Autom. Control* **1974**, *19*, 716–723. [CrossRef]
165. Freedman, W.L.; Madore, B.F.; Hatt, D.; Hoyt, T.J.; Jang, I.S.; Beaton, R.L.; Burns, C.R.; Lee, M.G.; Monson, A.J.; Neeley, J.R.; et al. The Carnegie-Chicago Hubble Program. VIII. An Independent Determination of the Hubble Constant Based on the Tip of the Red Giant Branch. *arXiv* **2019**, arXiv:1907.05922.
166. Coleman, S.R. The Fate of the False Vacuum. 1. Semiclassical Theory. *Phys. Rev. D* **1977**, *15*, 2929–2936. Erratum in *Phys. Rev. D* **1977**, *16*, 1248. [CrossRef]
167. Callan, C.G., Jr.; Coleman, S.R. The Fate of the False Vacuum. 2. First Quantum Corrections. *Phys. Rev. D* **1977**, *16*, 1762–1768. [CrossRef]
168. Patwardhan, A.V.; Fuller, G.M. Late-time vacuum phase transitions: Connecting sub-eV scale physics with cosmological structure formation. *Phys. Rev. D* **2014**, *90*, 063009. [CrossRef]
169. Niedermann, F.; Sloth, M.S. Resolving the Hubble tension with new early dark energy. *Phys. Rev. D* **2020**, *102*, 063527. [CrossRef]
170. Liddle, A.R. How many cosmological parameters? *Mon. Not. Roy. Astron. Soc.* **2004**, *351*, L49–L53. [CrossRef]
171. Arevalo, F.; Cid, A.; Moya, J. AIC and BIC for cosmological interacting scenarios. *Eur. Phys. J.* **2017**, *C77*, 565. [CrossRef]

172. Schwarz, G. Estimating the Dimension of a Model. *Annals Statist.* **1978**, *6*, 461–464. [CrossRef]
173. John, M.V.; Narlikar, J.V. Comparison of cosmological models using bayesian theory. *Phys. Rev. D* **2002**, *65*, 043506. [CrossRef]
174. Nesseris, S.; Garcia-Bellido, J. Is the Jeffreys' scale a reliable tool for Bayesian model comparison in cosmology? *J. Cosmol. Astropart. Phys.* **2013**, *8*, 36. [CrossRef]
175. Jeffreys, H. *Theory of Probability*, 3rd ed.; Oxford University Press: Oxford, UK, 1961.
176. Bonilla Rivera, A.; García-Farieta, J.E. Exploring the Dark Universe: Constraints on dynamical Dark Energy models from CMB, BAO and growth rate measurements. *Int. J. Mod. Phys. D* **2019**, *28*, 1950118. [CrossRef]
177. Pérez-Romero, J.; Nesseris, S. Cosmological constraints and comparison of viable $f(R)$ models. *Phys. Rev. D* **2018**, *97*, 023525. [CrossRef]
178. Camarena, D.; Marra, V. Impact of the cosmic variance on H_0 on cosmological analyses. *Phys. Rev. D* **2018**, *98*, 023537. [CrossRef]
179. Rezaei, M.; Malekjani, M.; Sola, J. Can dark energy be expressed as a power series of the Hubble parameter? *Phys. Rev. D* **2019**, *100*, 023539. [CrossRef]